

©2019
MARISSA S. BERGER
ALL RIGHTS RESERVED

A PHANTOM BASED STUDY OF SHORT-WAVE INFRARED EMITTING
NANOCOMPOSITES AS CONTRAST AGENTS FOR FLUORESCENCE
GUIDED SURGERY

By

MARISSA S. BERGER

A thesis submitted to the

School of Graduate Studies

Rutgers, The State University of New Jersey

In partial fulfillment of the requirements

For the degree of

Master of Science

Graduate Program in Biomedical Engineering

Written under the direction of

Mark C. Pierce, Ph.D.

And approved by

New Brunswick, New Jersey

May 2019

ABSTRACT OF THE THESIS

A Phantom Based Study of Short-Wave Infrared Emitting Nanocomposites as Contrast

Agents for Fluorescence Guided Surgery

By **MARISSA S. BERGER**

Thesis Director:
Mark C. Pierce, Ph.D.

Accurate, real-time detection and characterization of cancerous lesions is essential for effective surgical resection that both minimizes the chance of recurrence and preserves healthy tissue. In multiple ongoing clinical trials, optically-guided surgical techniques are utilizing fluorescent probes that emit light in the near infrared (NIR) window. Use of NIR light is motivated by lower scattering and autofluorescence in biological tissues than UV or visible light which results in improved imaging depth, contrast, and resolution. Because scattering monotonically decreases with increasing wavelength, several groups have hypothesized that probes emitting at the longer wavelengths in the short-wave infrared (SWIR) window may enable even deeper tissue imaging and greater resolution / contrast.

This thesis is focused on engineering an imaging system for fluorescence guided surgery in small animal models using SWIR-emitting human serum albumin encapsulated rare-earth nanocomposites (ReANCs). LabVIEW software controls the illumination, scanning, and imaging hardware components and provides real-time visualization of SWIR emissions overlaid on anatomical (white light) images. A separate Matlab

graphical user interface (GUI) was developed to enable quantitative post-processing of images acquired from the SWIR platform.

To validate the SWIR imager, a phantom study comparing the attainable imaging depth and resolution when using ReANCs versus the FDA-approved NIR fluorophore indocyanine green (ICG) versus white light was conducted. Tissue-mimicking gelatin phantoms were created with embedded agarose inclusions containing the contrast agent of interest. Inclusion depth, size, and shape were all varied, and inclusion contrast was quantified from SWIR and NIR images of the intact phantoms. Post-imaging, the inclusions were resected under SWIR, NIR, or white light guidance. The resected inclusions and inclusion cavities were then imaged to analyze resection accuracy for each guidance method.

A pilot *in vivo* animal study was performed using female athymic homozygous nude mice injected with Erbium-doped ReANCs. Imaging with the SWIR setup provided insight into future animal work. The cumulative findings of this thesis lay the groundwork for the design of a real-time imager that facilitates fluorescence-guided, deep tissue surgery, which has the potential to improve accuracy of tumor resection and decrease the chance of cancer recurrence.

ACKNOWLEDGEMENTS

I would like to acknowledge my thesis advisor Dr. Mark Pierce who has guided and supported me throughout the course of my M.S. degree. His mentorship has shaped me as an engineer and laid the groundwork for my career in biomedical engineering. I am deeply grateful for my experience working with Dr. Pierce. Thank you for everything you have done for me.

Next, I would like to thank my committee members Dr. Ilker Hacıhaliloğlu and Dr. Nada Boustany. Their insights and expertise in imaging and image analysis have vastly improved the quality of this work.

I would also like to thank our collaborator Dr. Vidya Ganapathy who has provided vast insights into the applications of this work in small animal and surgical imaging. Her guidance has been instrumental in bringing the project to fruition and in the design of both the phantom study and animal work. I would also like to thank Harini Kantamneni for assisting in the animal imaging work, and I wish her all the best going forward. Thank you as well to Jay Shah and Carolina Bobadilla-Mendez who have assisted me with the rare earth and optical imaging aspects of this project respectively. I am grateful that this project will continue in their capable hands.

Finally, I would like to thank my family and friends who have provided me with a continuous support system. To my friends in the Rutgers graduate program, thank you for encouraging me in my thesis work. To my best friend Malavika, thank you for being there for me all these years. To my parents Catherine and Michael Berger, thank you for believing in me and backing me. I could not have accomplished any of this without your

guidance. For all those who I have not mentioned but who have guided me in my journey,
I thank you.

DEDICATION

This thesis is dedicated to my parents Catherine and Michael Berger who have provided me with unwavering love and support. Through them, I gained the strength and ability to complete graduate school and the confidence to succeed in my future endeavors. I love you both more than anything.

I also dedicate this work to my friends who have been steadfast in their support and encouragement throughout my academic endeavors. Thank you for giving me the confidence to persevere.

TABLE OF CONTENTS

ABSTRACT OF THE THESIS	ii
ACKNOWLEDGEMENTS	iv
DEDICATION	vi
TABLE OF CONTENTS	vii
LIST OF TABLES	ix
LIST OF FIGURES	x
CHAPTER 1: INTRODUCTION	1
1.1: Cancer and Standard Treatments	1
1.2: Fluorescence-Guided Surgery	2
1.2.1: Concepts in Fluorescence Imaging	4
1.2.2: Commercial Surgical Guidance Systems and Contrast Agents	8
1.3: Short-Wave Infrared Light	12
1.4: Rare Earth Nanocomposites	16
1.4.1: Composition	16
1.4.2: Advantages	18
1.5: Aims	19
1.5.1: Motivation	19
1.5.2: Overview	19
1.6: Hypothesis	20
CHAPTER 2: INSTRUMENT DESIGN	21
2.1: Hardware	21
2.1.1: SWIR Emission Filters	21
2.1.2: Illumination of Rare Earth Phantoms	27
2.1.3: Illumination of ReANC and ICG Phantoms	30
2.1.4: Final Design	32
2.2: Software	34
CHAPTER 3: PHANTOM STUDY	38
3.1: ReANC Synthesis	38
3.2: Agarose-Gelatin Phantoms	39
3.2.1: Rationale	39
3.2.2: Fabrication	40
3.3: Chicken Breast Experiments	42
3.4: Inclusion Size and Depth Experiments	46

3.4.1: Phantom Design	47
3.4.2: Methods	47
3.4.3: Imaging Results	49
3.5: Inclusion Scattering and Resolution Experiments	52
3.5.1: Phantom Design	53
3.5.2: Methods	53
3.5.3: Imaging Results	55
3.5.4: Resection Results	59
3.6: Inclusion Shape Experiments	63
3.6.1: Phantom Design	64
3.6.2: Methods	64
3.6.3: Imaging Results	65
3.6.4: Resection Results	67
3.7: Discussion	68
3.7.1: Discussion of Imaging Results	68
3.7.2: Discussion of Resection Results	72
CHAPTER 4: CONCLUSIONS	73
4.1: Discussion of Results and Comparison to Literature	73
4.2: Future Direction	77
4.2.1: Small Animal Imaging	77
4.3: Summary and Conclusions	80
REFERENCES	82

LIST OF TABLES

Table 1: Factors that impact SBR in FGS.	5
Table 2: Optical filters tested for SBR optimization, listing the manufacturer, part number, transmission range, filter ID, and filter type.	21
Table 3: Summary of experimental parameters used for imaging ICG and erbium ReANC based phantoms.	34
Table 4: Mean pixel values for different regions of a uniform nanoparticle-laden phantom imaged under 0.026 W 980 nm collimated laser light. The lower left corner demonstrates decreased illumination intensity compared to the other illuminated regions.	52
Table 5: Peak heights and widths for ICG-containing and ReANC-containing inclusions at depths 1 mm, 3 mm, and 5 mm under 980 nm and 793 nm illumination.....	59
Table 6: Inclusions containing ICG were able to be resected at every depth using NIR guidance. The two shallowing ReANC-containing inclusions were able to be resected under SWIR guidance while the 5 mm depth inclusion was indistinguishable from the background and could not be resected. Control inclusions containing no contrast agent were resected under visual inspection and with guidance by palpation at every depth.	60
Table 7: Mean pixel values and SBRs for resected inclusions and cavities remaining after resection with NIR guidance (ICG inclusions) and SWIR guidance (ReANC inclusions). The SBR tended to be higher for the ICG-containing inclusions.	62
Table 8: Background-corrected mean pixel values and SBRs for irregularly-shaped and spherical inclusions containing 0.6 mg/mL ReANCs and placed 1 mm and 3 mm deep into a tissue-simulating gelatin phantom. Standard deviations represent the variation in six consecutive images of the phantom.	66
Table 9: Background-corrected mean pixel values and SBRs for resected irregularly-shaped and spherical inclusions and their cavities.....	67
Table 10: Mean pixel values for the liver of two female nude mice pre- and post-injection with 2 mg/mL Er-doped ReANCs. Values were found using both the novel LabVIEW-based software (Section 2.2) and the Sensors Unlimited Inc. (SUI) software provided with the camera. Corrected post-injection mean pixel values were calculated by subtracting the mean pre-injection pixel value from the mean post-injection pixel value. Values were in agreement for both platforms.	80

LIST OF FIGURES

Figure 1: Cetuximab-IRDye800 labeling of EGFR+ head and neck tumors. Reproduced from [34] with permission from the American Association for Cancer Research.....	3
Figure 2: Interactions of excitation and emission light with biological tissue. Excitation light (red) propagates through the tissue to excite the probe-labeled mass (blue). The pink arrow represents specular reflectance of the excitation light off the tissue surface. The dark blue spheres represent absorption events. The green stars represent scattering events while the arrows stemming from them indicate the direction of the scattered light. The purple mass represents tissue autofluorescence. The blue mass represents the probe-tagged region of interest while the blue arrows represent probe emissions.....	6
Figure 3: Commercial FGS imagers with characteristic display screen(s) and overhead illumination and detection features (Reproduced from [35] with permission from Taylor & Francis). The PDE Neo and Fluobeam use portable, handheld probes for fluorescence imaging [7,35]......	9
Figure 4: SWIR-emitting: (A) SWNTs (red) (reproduced from [33] with permission from Springer Nature) and (B) Quantum Dots (reproduced from [32] with permission from Springer Nature). The SWNTs' broad emission peaks prevent multispectral imaging while quantum dots can be precisely tuned to generate different emission peaks.	15
Figure 5: (A) Rare earth nanoparticle structure showing lanthanide- and Yb ³⁺ -doped NaYF ₄ core with undoped NaYF ₄ shell. (B) ReANC structure demonstrating albumin encapsulation of the rare earth nanoparticles. Reproduced from [21] with permission from Springer Nature.....	16
Figure 6: Emission spectra for differently-doped rare earth nanoparticles yield four distinct peaks. Reproduced from [21] with permission from Springer Nature.	17
Figure 7: Erbium emission spectrum (green) with 980 nm excitation (red).	22
Figure 8: (A) ROI selection of the signal from a nanoparticle-laden phantom and (B) background from a control (nanoparticle-free) phantom using a Xenon-Topaz f/#2.0 lens (Schneider Optics) and BLP01-980R-25 filter (Semrock). The exposure time was 16.83 ms, and the illumination wavelength was 980 nm. Images depict signal values with the laser turned on.....	24
Figure 9: SBR and % Transmission values for different filter combinations (see Table 2 definitions) tested with a VIS-NIR lens. Error bars represent the propagated error of the standard deviations of pixel values in each ROI. All combinations with the 1538/82 bandpass filter have comparable SBR and %T values. Their SBR values are significantly higher than those for filter sets without the 1538/82 nm bandpass filter except for the 1550 nm bandpass filter.	25
Figure 10: SBR and % Transmission values for different filter combinations (see Table 2 definitions) tested with a SWIR lens. Error bars represent the propagated error of the standard deviations of pixel values in each ROI. All combinations with the 1538/82 bandpass filter have comparable SBR and %T values. Their SBR values are significantly higher than those for filter sets without the 1538/82 nm bandpass filter.	25

Figure 11: Filter Transmission values for the FF01-832-37 bandpass filter (Semrock) in comparison to the absorption and emission spectra of ICG. The FF01-832-37 best maximizes the transmission of light around ICG's peak emission wavelength (840 nm) while minimizing transmission at the excitation laser wavelength.	27
Figure 12: Field of illumination for an Erbium nanoparticle-laden phantom with varying distance between laser and sample demonstrates an increase in illumination area with distance from the sample. (A) Distance 24.91 cm, Diameter 7.04 cm; (B) Distance 27.20 cm, Diameter 7.69 cm; (C) Distance 29.54 cm, Diameter 8.35 cm; (D) Distance 31.89 cm, Diameter 9.02 cm; (E) Distance 32.78 cm, Diameter 9.27 cm; (F) Distance 35.10 cm, Diameter 9.93 cm; (G) Distance 37.44 cm, Diameter 10.59 cm; (H) Distance 38.36 cm, Diameter 10.85 cm; (I) Distance 40.67 cm, Diameter 11.50 cm; (J) Distance 43.00 cm, Diameter 12.16 cm. Images captured were 12-bit.	30
Figure 13: Experimentally-measured average pixel intensity decreases with area illuminated in agreement with theoretically-predicted values according to the relationship $I = P/A$. Data were generated from 12-bit images.	30
Figure 14: Final setup for SWIR imaging consisting of a collimated 980 nm laser for illumination and an InGaAs SWIR-detecting camera equipped with a lens and filters for detection. Arrows indicate the position of the camera and illumination source.	33
Figure 15: (A) Final setup for NIR imaging consisting of a collimated 785 nm laser for illumination and an sCMOS NIR-detecting camera equipped with a lens and filters for detection. Arrows indicate the position of the camera and illumination source. (B) The illumination spectrum of the NIR laser is centered at 793 nm when equipped with a tilted 800 nm bandpass filter (Thorlabs, FB800-10).	34
Figure 16: Software display screen showing: (1) a control panel, (2) The running image, (3) the fluorescent image, (4) the real-time overlay, and (5) the white light image.	37
Figure 17: 5 mm diameter agarose inclusions containing Er-doped ReANCs, formed in in 3D printed molds.	41
Figure 18: White light (top) and SWIR overlay (bottom) images of a 5 mm diameter agarose inclusion containing an ReANC concentration of 0.6 mg/mL beneath chicken breast of thicknesses 1.6 mm, 2.5 mm, and 5 mm. Yellow arrows point to detected signals from the inclusion. Signal intensity decreased with chicken breast thickness, and at 5 mm, no signal was discernible by visual inspection.	43
Figure 19: Summary of raw and background-corrected average pixel intensities for 12-bit images of a 5 mm diameter Er ReANC-containing inclusions placed below varying thicknesses of chicken breast. As chicken breast thickness increased, average pixel intensity of the signal decreased.	44
Figure 20: SWIR images of a 5 mm diameter agarose inclusion containing an ReANC concentration of 0.6 mg/mL below chicken breast of thicknesses 1 mm, 2 mm, 3 mm, 4 mm, 5 mm, 6 mm, and 8 mm. Yellow arrows point to detected signals from the inclusion. Signal intensity decreased with chicken breast thickness, and at 6 mm, no signal was discernible by visual inspection.	45
Figure 21: Summary background-corrected average pixel intensities for 12-bit images of a 5 mm diameter Er-doped ReANC-containing inclusions placed below varying thicknesses of	

chicken breast. As chicken breast thickness increased, average pixel intensity of the signal decreased and dropped down to background level at 6 mm thickness.	45
Figure 22: Summary SBR for 12-bit images of a 5 mm diameter Er ReANC-containing inclusions placed below varying thicknesses of chicken breast. As chicken breast thickness increased, SBR of the signal decreased and dropped down to 1 at 6 mm thickness.....	46
Figure 23: Design of size-depth testing phantom showing agarose inclusions of 5 mm, 7.5 mm, and 10 mm diameters placed at depths between 1 mm and 5 mm within a gelatin phantom. One corner is notched to determine orientation upon imaging.	47
Figure 24: Size-depth phantom containing 0.6 mg/mL ReANC agarose inclusions of 5 mm, 7.5 mm, and 10 mm diameter embedded at depths of 1 mm, 3 mm, and 5 mm. The notched corner indicates orientation.	48
Figure 25: White light, SWIR overlay, and contrast adjusted SWIR images of a size-depth phantom containing 0.6 mg/mL ReANC agarose inclusions of 5 mm, 7.5 mm, and 10 mm diameter embedded at depths of 1 mm, 3 mm, and 5 mm. The phantom was imaged at two orientations (0 and 180 degree rotations) to take into account variations in scanning illumination. The SWIR image contrast was enhanced to better visualize the 3 mm deep signals. Red arrows indicate progression of inclusion depth and size. Yellow arrows indicate regions of fluorescent signal intensity. The raw SWIR image had a range of pixel values between 0 and 4095, and the contrast adjusted SWIR image was scaled between values 40 and 500 for display only.	49
Figure 26: Background corrected mean pixel values for 5 mm, 7.5 mm, and 10 mm diameter 0.6 mg/mL ReANC agarose inclusions at 1 mm and 3 mm depths into a gelatin phantom. Different color bars indicate different scans of the same phantom. Values represent the mean pixel value for each inclusion minus the background mean pixel value. For the 0 degree orientation, the mean pixel value decreased with decreasing size. For the 180 degree orientation, a similar trend was observed with the exception of the 10 mm diameter inclusion at 1 mm deep.	50
Figure 27: SBR values for 5 mm, 7.5 mm, and 10 mm diameter 0.6 mg/mL ReANC agarose inclusions at 1 mm and 3 mm depths into a gelatin phantom. Values reported are averages of different scans of the same phantom in the same orientation. Error bars represent the standard deviation between different scans. SBR approaches 1 at 3 mm deep for all three sized diameters, indicating a 3 mm limiting depth.....	50
Figure 28: White light and SWIR images of a uniform nanoparticle-laden phantom scanned with a 0.026 W 980 nm collimated laser and the accompanying histogram of the whole phantom ROI. The %CV for the pixel values across the region was 28%, indicating a significant variation in the illumination intensity.	51
Figure 29: Phantom fabrication process for evaluation of scattering and resolution. Spherical inclusions of 10 mm diameter were placed at depths 1 mm, 3 mm, and 5 mm into a tissue-mimicking gelation phantom. Inclusions contained either no contrast agent (agarose only controls), 14 μ M ICG, or 0.6 mg/mL Er-doped ReANCs.....	54
Figure 30: White light, overlay, and SWIR images of the ICG-ReANC composite phantom illuminated using the SWIR hardware and software described in Section 2.1.4 and Section 2.2. Under 980 nm / 1.8 W illumination, only the 1 mm and 3 mm deep	

inclusions were discernible. The ICG-containing inclusions did not emit a detectable signal in Er's emission range. Yellow arrows indicate inclusion positions. The red arrow indicates the direction of increasing inclusion depth. The raw SWIR image had a range of potential pixel values between 0 and 4095, and the contrast adjusted SWIR image was scaled between values 50 and 200 for display only.	56
Figure 31: White light, overlay, and NIR images of the ICG-ReANC composite phantom illuminated using the NIR hardware and software described in Section 2.1.4 and Section 2.2. Under 793 nm 12 mW (380 mA) illumination, inclusions at every depth were detected for both contrast agents, suggesting that the ReANC-containing inclusions emit a detectable signal in ICG's emission range. Yellow arrows indicate inclusion positions. The red arrow indicates the direction of increasing inclusion depth.....	56
Figure 32: (A) Corrected mean pixel values for the NIR and SWIR emissions from ICG-containing and ReANC-containing inclusions at concentrations 14 μ M and 0.6 mg/mL respectively at 1 mm, 3 mm, and 5 mm depths under 980 nm and 793 nm illumination. (B) The corresponding SBR values. The NIR emissions from both inclusions had higher mean pixel values and SBRs than the SWIR emissions from the ReANC-containing inclusions. Results indicate that ICG NIR emissions are the most distinguishable from background. Error bars indicate one standard deviation from the mean of the six images in each set.....	58
Figure 33: Line intensity profiles of the NIR and SWIR emissions from ICG-containing (14 μ M) and ReANC-containing (0.6 mg/mL) inclusions at 1 mm, 3 mm, and 5 mm depths under 980 nm and 793 nm illumination. Red bars indicate the full width at half maximum peak height. The raw SWIR image had a range of pixel values between 0 and 4095, and the shown SWIR image was scaled between values 50 and 200 for display only.	58
Figure 34: Flipping the ICG-ReANC composite phantom over reverses the inclusion depths, allowing the ReANC-containing inclusion previously at 5 mm deep to be imaged as a 1 mm deep inclusion. The raw SWIR images had a range of pixel values between 0 and 4095, and the contrast adjusted SWIR images were scaled between values 50 and 200 for display only.	60
Figure 35: Resected phantoms and ReANC-containing inclusions under SWIR guidance with fluorescence images. Yellow arrows point to the positive margins in the cavities. The red arrow and text indicate the depth at which the inclusion was placed. Blue dashed arrows indicate the cavity from which the indicated inclusion was resected. The raw SWIR images had a range of pixel values between 0 and 4095, and the contrast adjusted SWIR images were scaled between values 50 and 200 for display only.	61
Figure 36: Resected phantoms and ICG-containing inclusions under NIR guidance with fluorescence images. Yellow arrows point to the positive margins in the cavities. The red arrow and text indicate the depths at which the inclusions were placed. Blue dashed arrows indicate the cavity from which the indicated inclusion was resected. NIR pixel values were in the range of 0 to 4095.	62
Figure 37: Resected phantoms and probe-free inclusions under visible light and palpation guidance. The red arrow and text indicate the depth at which the inclusion was placed. Blue dashed arrows indicate the cavity from which the indicated inclusion was resected.	63

Figure 38: Custom molds (left) were 3D-printed and filled with agarose mixtures to produce inclusions of irregular shape (right).	64
Figure 39: Phantom design for comparisons between irregularly-shaped and spherical ReANC-containing inclusions of 7.5 mm diameter placed 1 mm and 3 mm deep into a tissue-mimicking gelatin phantom.....	65
Figure 40: White light, overlay, and SWIR images of 7.5 mm diameter ReANC-containing spherical and irregularly-shaped inclusions at 0.6 mg/mL concentration and depths of 1 mm and 3 mm. The irregularly shaped inclusion is visibly non-spherical at 1 mm deep but not detectable at 3 mm deep. The raw SWIR image had a range of pixel values between 0 and 4095, and the contrast adjusted SWIR image was scaled between values 50 and 200 for display only.....	66
Figure 41: White light and SWIR images of the imaged cavity and inclusions show highest positive margins for the irregularly-shaped inclusion at 1 mm depth. SWIR pixel values ranged between 0 and 4095.....	67
Figure 42: (A) Quantum efficiency for the NIR-sensitive Zyla 5.5 sCMOS camera (Andor) [39]. (B) Quantum efficiency for the SWIR-sensitive SUI640HSX-1.7RT camera (Sensors Unlimited) [40].	69
Figure 43: Absorption spectra for water (green), deoxy-hemoglobin (blue) and oxy-hemoglobin (red). Reproduced from [41] with permission from AIP Publishing.	70
Figure 44: Absorption spectra measured for varying athymic nude mouse tissues indicate lowest absorption of 1525 nm light in the lungs and bone tissue. Reproduced from [21] with permission from Springer Nature.....	74
Figure 45: White light, SWIR, and overlay images of a female nude mice taken pre- and post-injection of 2 mg/mL Er-doped ReANCs using the novel SWIR imaging system (Section 2.1.4 and 2.2). The yellow arrow indicates the SWIR signal from the liver. Weaker fluorescent signal from the vasculature is apparent in both SWIR post-injection images as the time between imaging and injection was too short to allow all ReANCs to clear. 78	
Figure 46: White light, SWIR, and overlay images of a female nude mice taken post-injection of 2 mg/mL Er-doped ReANCs using the Sensors Unlimited Inc. (SUI) software. Values were colormapped between 20 and 200.	79

CHAPTER 1: INTRODUCTION

This thesis focuses on the design of a surgical guidance system for use with short-wave infrared (SWIR) light-emitting rare earth nanocomposites and its validation against a near infrared (NIR) light-based system using tissue simulating phantoms. The ultimate goal of the broader project is to develop an imaging platform with real-time capabilities for guiding surgeons in identifying cancerous lesions during resection.

1.1: Cancer and Standard Treatments

Cancer, the second leading cause of death in the United States, is defined as an uncontrolled growth and spread of abnormal cells, and among women, breast cancer is the most common form [1-3]. As with most solid tumor cancers, the primary treatment is surgical resection with negative margins, in which the cancerous tissue is completely excised from the body [4]. Until recently, most cases resulted in mastectomies, where the entire breast is removed. However, with the emergence of better diagnostic tools that can identify smaller, localized tumors early on, there has been a transition to breast-conserving therapies, like lumpectomies [5]. Breast-conserving surgeries produce more cosmetically-appealing results by excising cancerous regions with a relatively small margin of healthy tissue [5]. For this reason, patient outcome and risk of recurrence depend on accurate margin identification. Gold standard techniques for intraoperative margin assessment, such as visual inspection and palpation, ultrasound, and frozen section pathology, are commonly used methods, but their accuracy is limited [4]. Cancerous and healthy tissues are difficult to distinguish under visible light conditions, and primary surgical resection is susceptible to positive margins, areas of remaining

cancer cells, with 20-40% of breast cancer patients experiencing positive margins after surgery [6]. Positive margins coincide with increased risk of local recurrence, need for re-excision, higher costs, poorer prognosis, and overtreatment [4]. Intraoperative imaging techniques aim to enable surgeons to better visualize cancerous tissue, minimizing risk of these complications.

The most common intraoperative imaging modality is ultrasound, which is limited in resolution [4]. Other techniques, like computed tomography (CT) and MRI provide better anatomical resolution but are costly and poorly suited to real-time imaging, which is necessary for surgical guidance [4]. Optical imaging techniques may present a high-resolution method of real-time intraoperative margin assessment in a safer and more cost-effective manner.

1.2: Fluorescence-Guided Surgery

Fluorescence-guided surgery (FGS) is an optical imaging technique that employs fluorescent probes or contrast agents. During excitation, these probes absorb incident light, and their electrons shift to a higher energy state. As these electrons return to the ground state, they emit energy as photons, which generally have longer wavelengths than the illumination source due to energy loss in the excited state.

When fluorescent probes are administered to a patient, they can accumulate at an area of interest within the body in two fundamental ways. Untargeted probes accumulate passively through the enhanced permeability and retention (EPR) effect, taking advantage of the abundance of “leaky” blood vessels in tumors, distinguished by wide fenestrations between endothelial cells. Probes in the blood stream can easily penetrate into the tumor

space through these wide openings and are retained longer than in healthy tissue due to poor lymphatic drainage, which characterizes most tumors. However, the contrast agent is still free to transverse back through the tumor space and into the vasculature, limiting tumor retention. Targeted probes, on the other hand, contain functional moieties, like antibodies or peptides, that allow them to bind to specific biomarkers expressed by the cancer cells of interest. Like untargeted probes, they accumulate at the tumor by flowing through the leaky vasculature, but afterwards, they bind selectively to the cancer cell biomarkers, preventing their immediate return to the bloodstream. By administering and exciting these targeted probes within a patient, one can visualize more clearly the tumor boundaries.

In FGS, a light source such as a laser diode or light-emitting diode (LED), illuminates the tissue and excites the probes [7]. Emissions propagate out of the tissue and through selective optical filters, which block wavelengths outside the probe's emission range [7]. These emissions can be captured on a camera, generating an image of fluorescent probe distribution that can displayed on screen in real-time [7].

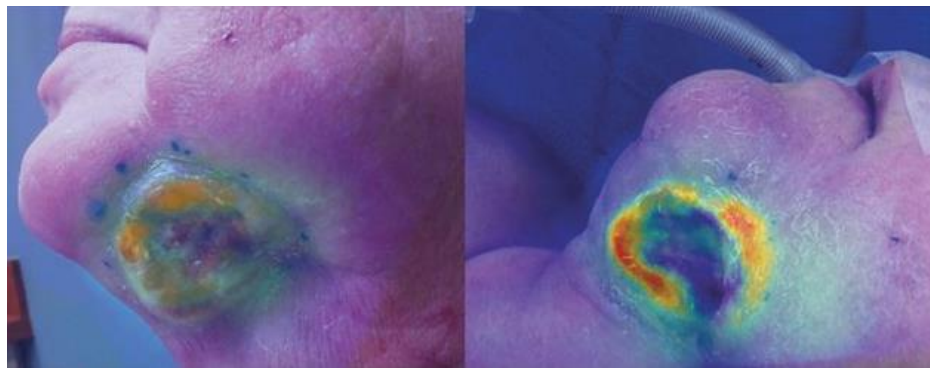


Figure 1: Cetuximab-IRDye800 labeling of EGFR+ head and neck tumors. Reproduced from [34] with permission from the American Association for Cancer Research.

Image pixel intensity is dependent on the local concentration of contrast agent in the tissue, with areas of high probe accumulation generating a higher intensity signal. In this way, FGS creates contrast between areas of high and low probe concentration. Probes targeted to cancer cells will preferentially concentrate at tumor sites and increase contrast between cancerous and healthy tissue, thereby allowing surgeons to better distinguish lesions during resection.

1.2.1: Concepts in Fluorescence Imaging

The goal of FGS systems is to achieve high contrast between healthy and cancerous tissue, thereby improving tumor visualization and margin assessment accuracy. To accomplish this, FGS systems aim to maximize the signal-to-background ratio (SBR), the ratio of emission intensity from the cancerous tissue (signal) to that of healthy tissue (background) [7]. Doing so requires an awareness of all the factors that impact SBR in FGS (Table 1).

Table 1: Factors that Influence SBR in FGS	
Factor	Definition
Light Absorption in Tissue	Conversion of probe excitation and emission beams to heat energy
Light Scattering in Tissue	Deviation of excitation and emission beams from incident paths
Tissue Autofluorescence at Excitation Wavelength	Fluorescent emissions from biological tissue under the excitation wavelength
Probe Absorption Cross-Section at Excitation Wavelength	Probability of the probe absorbing light at the excitation wavelength
Probe Specificity	Selectiveness of the probe for the target biomarker
Probe Quantum Efficiency	Probability of an incident excitation photon generating an emitted photon
Incident Excitation Intensity	Optical excitation power per unit area at the site of probe accumulation
Camera Quantum Efficiency	Efficiency of converting incident photons to photoelectrons at each pixel

Camera Noise	Random variation in pixel values due to shot noise, thermal (dark) noise, and read noise
Lens f-Number	A measure of the light collecting ability of a lens
Filter OD in the Blocking Region	Wavelength-dependent degree of light attenuation by a filter
Filter % Transmission in the Transmission Region	Wavelength-dependent percentage of light passing through a filter

Table 1: Factors that impact SBR in FGS.

An ideal FGS system utilizes excitation and emission wavelengths that attenuate minimally while travelling through the tissue. Light experiences two main attenuating events in biological tissue: it can scatter off tissue inhomogeneities, diverting from its original path, or it can be absorbed and converted to heat energy [8]. As excitation light attenuates, its intensity diminishes. Excitation wavelengths that attenuate more through tissue have lower intensity when they reach the fluorescent probes. When excitation intensity is low, the emission intensity is also low and the SBR falls. As emission photons propagate and undergo multiple scattering events, they reach the detector at positions incongruent with the object's geometry, blurring the image. With a large enough scattering angle, photons may even miss the lens' collection cone completely, lowering the number of photons detected and the signal intensity. Alternatively, probe emissions can be absorbed, decreasing the photon count at the detector. Both events lower SBR by lowering signal intensity closer to the background intensity.

The surrounding tissue also affects image quality in FGS. Some components of biological tissue naturally exhibit autofluorescence [8]. These emissions are included in the detected signal, decreasing the SBR and worsening the contrast between normal and cancerous tissues. In a similar manner, backscattered light from the illumination source

can raise the background level in an image if not sufficiently blocked from detection [7]. Thus, to achieve a high SBR, FGS must use optical probes whose excitation and emission wavelengths are distinct from each other, experience minimal scattering and absorption in biological tissue, and produce little to no autofluorescence.

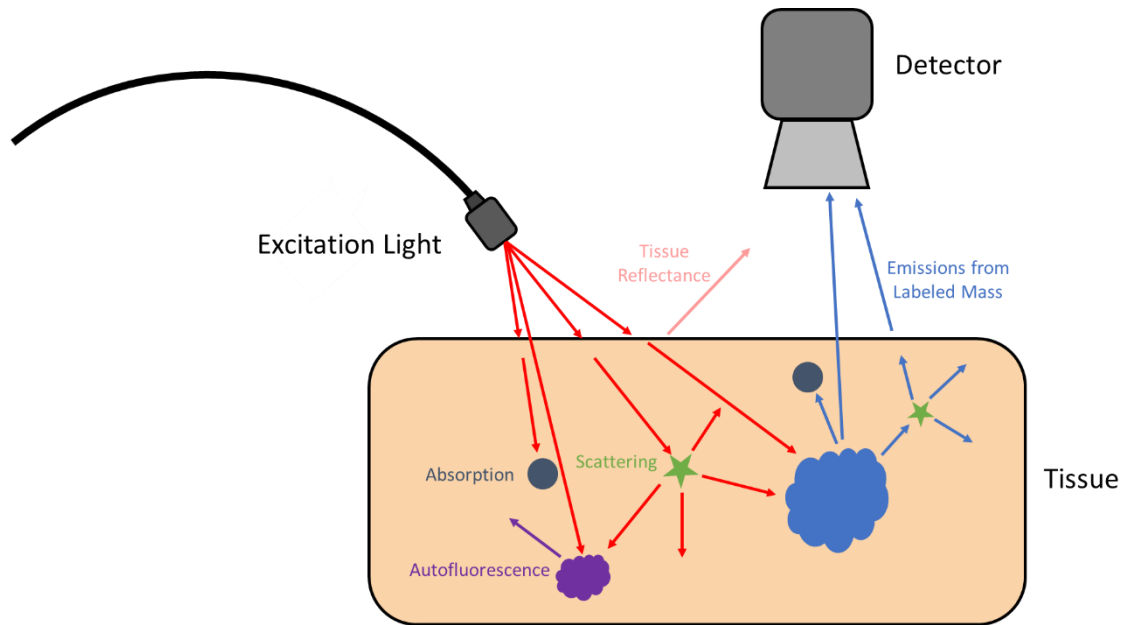


Figure 2: Interactions of excitation and emission light with biological tissue. Excitation light (red) propagates through the tissue to excite the probe-labeled mass (blue). The pink arrow represents specular reflectance of the excitation light off the tissue surface. The dark blue spheres represent absorption events. The green stars represent scattering events while the arrows stemming from them indicate the direction of the scattered light. The purple mass represents tissue autofluorescence. The blue mass represents the probe-tagged region of interest while the blue arrows represent probe emissions.

Fluorescence imaging typically employs ultraviolet (UV) (200-400 nm), visible (400-700 nm), or near infrared (NIR) (700-1000 nm) light [9-10]. Early FGS probes exhibited excitation and emission wavelengths in the visible range. In recent years, the focus of FGS has shifted towards the NIR which presents two distinct advantages: its longer wavelengths scatter and absorb less in biological tissue, thereby allowing resolution of deeper set targets, and NIR excitation causes less tissue autofluorescence,

enabling a higher SBR [9-10]. For instance, the visible light-emitting probe fluorescein isothiocyanate (FITC) (519 nm emission peak) was the first to enable surgeons to stage and visualize folate receptor α -positive ovarian cancer lesions in humans but was limited by its poor penetration depth [11]. In pulmonary adenocarcinoma studies, NIR-emitting OTL38 (795 nm emission peak) improved penetration depth over FITC from 1 mm to 10 mm into pleural tissue [12]. Another NIR contrast agent, IRDye800CW (794 nm emission peak), has recently been functionalized with the FDA-approved antibodies cetuximab and panitumumab and used for targeting EGFR in microscopic head and neck cancer resection. This NIR probe demonstrated increased SBR and reduced autofluorescence compared to the far-red emitting (710 nm emission peak) Cy5.5 [13-14]. It is now widely accepted that NIR light-based techniques are capable of higher resolution and deeper imaging than with visible or UV light due to their longer wavelengths.

Several research groups are exploring whether even deeper tissue imaging may be possible by going beyond the NIR range into the SWIR spectral region. Wang *et al.* found that the penetration depth of SWIR-emitting nanoparticles (DNCPS, 1060 nm emission peak) was 8 mm through a solution of water, PBS, blood, and serum at 37 °C, nearly three times that of NIR-emitting indocyanine green (ICG, 840 nm emission peak) [15]. Another study investigated the penetration depth of 750 nm, 1200 nm, 1700 nm, and 2200 nm light by imaging thin human prostate tissue, human breast tissue, and pig brain slices under each wavelength [16]. It was found that the penetration depths for all three SWIR wavelengths exceeded that of the 750 nm NIR light, with the 1700 nm light penetrating almost two times as far as the 750 nm light through prostate and breast tissue

[16]. In a follow-up experiment, Sordillo *et al.* trans-illuminated wires placed under chicken breast of varying thicknesses with NIR and SWIR light and evaluated each wavelength's transmission [16]. While NIR light (650 nm to 900 nm) could not penetrate far enough to provide an image of the wires, light in the second (1100 nm to 1350 nm) and third (1600 nm to 1870 nm) SWIR windows had a maximum penetration depth of 3.9 mm, with the second SWIR window providing the greatest contrast [16]. Based on these studies, the reduction in scattering going from the NIR to SWIR wavelengths may allow for improved contrast at greater depths. However, water absorption peaks strongly around 1444 nm and 1950 nm and will influence penetration depth greatly near those wavelengths [16].

1.2.2: Commercial Surgical Guidance Systems and Contrast Agents

A number of different commercial and research imagers are available for FGS with visible or NIR wavelengths. Their main components include: an illumination source, excitation and emission filters, light-collection optics, a high-sensitivity CCD or CMOS camera, and image display software [7,17-18].



Figure 3: Commercial FGS imagers with characteristic display screen(s) and overhead illumination and detection features (Reproduced from [35] with permission from Taylor & Francis). The PDE Neo and Fluobeam use portable, handheld probes for fluorescence imaging [7,35].

The excitation light source in an FGS system is commonly either a filtered broadband lamp, LED array, or laser diode(s) [7,17]. In selecting between them, one considers factors such as field of view (FOV), output brightness, and cost [7]. For surgical guidance, an ideal system maximizes FOV while minimizing cost and optimizing for the illumination intensity at the tissue. The system must operate at a power that ensures a high but safe illumination intensity, conforming to the American National Standards Institute (ANSI) guidelines for the safe use of lasers (z136.1). For practicality, the beam must cover a large enough area that a surgeon can view the whole ROI for the duration of the surgery without having to frequently adjust the beam location. Most open

surgery imaging systems offer an adjustable FOV, for which 10 cm to 20 cm is considered an ideal maximum FOV diameter (79 cm² to 314 cm² area) [7,17]. The FDA-approved SPY system (Novadaq), for instance, has an FOV range of 38 cm² to 241.2 cm² [17-18]. In small tumor resections specifically, the minimum FOV size is 1-2 cm in diameter (0.785 cm² to 3.14 cm²) [17].

In selection of the excitation beam wavelength, commercial imagers are optimized to obtain a high overall SBR. Illumination at the fluorescent probe's peak excitation wavelength excites the most probes, but for a probe with a small Stokes shift, illuminating at a wavelength shorter than the excitation peak may allow more emission light to be collected. For this reason, FGS systems are commonly tailored to match the excitation and emission properties of the select probe administered.

Upon excitation, probes emit a range of wavelengths around a peak emission wavelength; however, contributions from tissue autofluorescence, backscattered light from the excitation beam, and even surgical overhead lights can increase the measured background level and decrease the SBR. To maximize SBR and contrast between healthy and abnormal tissue, FGS systems have built-in filters that block wavelengths outside the range of interest from reaching the detector. Commonly-used filter types include longpass filters which pass wavelengths beyond a given cutoff, bandpass filters which pass a range of wavelengths, and notch filters which pass wavelengths outside a given range [7]. The choice of filter depends on both the excitation and emission range of the probe. It is desirable that wavelengths around the peak emission wavelength are passed so that a high signal intensity is captured while excitation light source wavelengths are blocked. For probes that have a small Stokes shift, it can be difficult to collect light over the entire

emission spectrum [7]. ICG for example, is a popular fluorescent imaging agent with an excitation peak of 800 nm and an emission peak of 840 nm in blood [19]. Because there is a high level of excitation and emission overlap with ICG, excitation source wavelength and emission filter selection are more difficult than with probes that experience less spectral overlap.

Once filtered, emissions are captured by a camera which maps the intensity of incident light to a range of digital pixel values. Most commercial imagers are NIR light-based and so use CCD cameras [7,17-18]. Traditionally, CCD sensors offered the highest sensitivities but sCMOS cameras have advanced dramatically in recent years, with back-thinned versions reaching the market and gaining popularity for NIR imaging [7,17].

Upon detection, fluorescent photons are converted to photoelectrons, then digitized to pixel values and displayed on a screen with real-time overlay of the fluorescent image on top of a white light image. The overlay allows surgeons to orient themselves to the anatomical information provided by the white light image while also better visualizing the probe's distribution from the fluorescent image.

With these factors in mind, it is necessary to note that many FGS systems are designed for use with ICG, which is a powerful fluorophore used in angiography and intraoperative sentinel lymph node mapping in breast cancer [7,17-18]. ICG is the primary contrast agent for NIR range imaging, in part due to its status as the first of only two FDA-approved NIR contrast agent for FGS [7]. It is an untargeted, water-soluble compound with excitation and emission peaks at 800 nm and 840 nm respectively in blood [19]. With both peaks in the NIR range, ICG has lower autofluorescence as compared to contrast agents with excitation wavelengths in the visible spectrum. The

standard dose in fluorescence imaging is 2.5 mg/ml intravenously, with up to 25 mg delivered in an adult, though ICG is often administered subcutaneously or intradermally in clinical lymphatic imaging [17]. ICG fluorescence intensity is nonlinear with concentration as ICG quenches at too high concentration, and Gioux *et al.* reported an ICG quenching threshold of 50 μM [17]. In tissue-mimicking phantom design, there is no set standard for ICG dose; however, Pleijhuis *et al.* reported an ideal concentration of 14 μM in agarose [20]. With all this in mind, when validating new contrast agents for surgical use, it is necessary to compare imaging performance with ICG, as this is the most clinically-mature FGS approach to-date.

1.3: Short-Wave Infrared Light

Short-wave infrared (SWIR) light encompasses wavelengths in the 1000 to 2300 nm range [21]. Due to its longer wavelength compared to the NIR, SWIR light has comparably low autofluorescence with further reduced scattering, which has been shown to improve resolution in turbid media [21]. It has been theorized that the lower scattering of SWIR light may extend penetration depth beyond that of NIR light, though water absorption, with peaks at around 1450 nm and 1900 nm, will reduce this impact for SWIR wavelengths in that range and past it where the peak's tail extends. A study by Hong *et al.* compared the penetration depth of SWIR and NIR light through tissue simulating phantoms composed of 1% Intralipid [22]. Capillary tubes were filled with either SWIR-emitting single walled carbon nanotube (SWNT)-IRDye800 conjugates (1350 nm emission peak) or NIR-emitting IRDye800 (800 nm emission peak) [22]. The capillary tubes were placed at depths of 1 mm and 10 mm beneath the tissue surface and

illuminated under 808 nm [22]. At 10 mm, scattering was evident for both SWIR and NIR emissions but more severe in the NIR window to the point where the tube was no longer visible [22]. Meanwhile, SWIR emissions experienced less scattering, especially in the 1300-1400 nm range, where sharp edges could still be resolved at 10 mm deep [22]. Based on this study, SWIR light in this range scatters less through tissue than NIR light, allowing for resolution of objects at greater depths. As scattering decreases with increased wavelength, it may be possible to achieve greater penetration depths for SWIR wavelengths beyond 1400 nm despite increased water absorption.

Comparisons between SWIR-emitting and NIR-emitting probes have shown that certain ranges of SWIR light have greater penetration depth than NIR light, and further investigation has demonstrated the improved resolution of SWIR over NIR. ICG has an emission peak in the NIR range, but its spectral tail extends into the SWIR, putting into question whether objects could be resolved better by capturing ICG's SWIR emissions. Starosolski *et al.* performed a similar experiment to Hong *et al.* comparing ICG's NIR and SWIR emissions. Capillary tubes containing 50 μM of ICG in bovine plasma were inserted at 1 mm to 5 mm deep into a 1% intralipid phantom, and their SWIR and NIR emissions measured by an InGaAs or silicon CCD camera equipped with appropriate filters [23]. SWIR emissions showed lower scattering compared to NIR light at depths above 1 mm, indicating better resolution at greater depths [23]. Repeating these experiments in chicken muscle and liver tissue, Starosolski *et al.* placed capillary tubes filled with either ICG or the SWIR-emitting IR-E1050 (1050 nm emission peak) in plasma or PBS at depths of 3 mm and 6 mm into the tissue [23]. Contrast to noise ratio (CNR), equal to the difference in SBR between a capillary tube in tissue and the region

next to the tube, was the metric used for comparison [23]. CNR decreased with depth for both windows except in the case of ICG in plasma in chicken, and overall, the SWIR emissions from ICG had the greatest CNRs at 6 mm deep, indicating better SBR and resolution in the SWIR range [23]. Thus, SWIR light may offer the advantage of higher resolution at greater depths, making it useful for deep tissue imaging.

Research into SWIR-emitting contrast agents is extensive. Quantum dots (QDs) are inorganic, nanoscale fluorophores whose emissions can be tuned to different SWIR wavelengths based on probe size (Figure 4B) [21,24]. These contrast agents offer targeting capabilities and a broad range of emission wavelengths that enable multispectral imaging, which is useful for differentiating between tissue types during FGS [21,24-25]. Still, the high toxicity of their cadmium cores poses a potential cytotoxicity issue that has prevented quantum dots from being used in humans [24].

Other potential SWIR contrast agents include single-walled carbon nanotubes (SWNTs, Figure 4A). SWNTs can be conjugated with targeting moieties but are capable of high untargeted uptake by cancer cells via the EPR effect [25-26]. Their large Stokes shift of 400 - 500 nm enables imaging with low background, and Robinson *et al.* report an intrinsic fluorescence in the 1100 nm to 1400 nm range [26]. With their SWIR emissions, SWNTs accommodate deep tissue imaging; however, their emission and excitation peaks are broad, preventing tunability and multispectral imaging [27]. Moreover, they are relatively long nanomaterials, making it difficult for them to penetrate size-limited biological barriers [27].

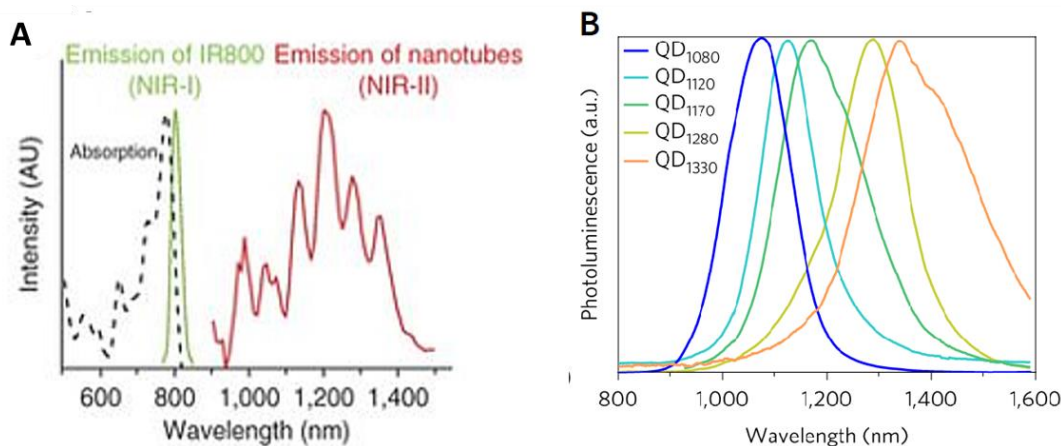


Figure 4: SWIR-emitting: (A) SWNTs (red) (reproduced from [33] with permission from Springer Nature) and (B) Quantum Dots (reproduced from [32] with permission from Springer Nature). The SWNTs' broad emission peaks prevent multispectral imaging while quantum dots can be precisely tuned to generate different emission peaks.

QDs exceeding a hydrodynamic radius of 5.5 nm tend to be retained by the body to a high degree post-imaging as their size prevents renal filtration [25]. In contrast, small-molecule SWIR-emitting organic dyes are more readily excreted from the body, decreasing long-term toxicity risks [25]. These dyes are typically water-insoluble and must be PEGylated to be biocompatible, but there are lingering toxicity concerns should there be leakage of the fluorescent agent through the amphiphilic coating [25].

SWIR-emitting rare earth-doped nanoparticles (RENPs) are contrast agents capable of targeted, multispectral imaging with low toxicity and a desirable uptake and biodistribution profile after albumin encapsulation [25]. They generate fluorescence through non-radiative energy transfer from a sensitizer ion to the rare earth dopant, allowing emissions to be tuned based on dopant identity [25]. RENPs have narrower emission peaks than SWNTs and quantum dots, that combined with their tunability, enhances their prospects for multispectral imaging [25]. Experiencing minimal

photobleaching, RENPs are prime agents for SWIR imaging over an extended period of time [25].

1.4: Rare Earth Nanocomposites

1.4.1: Composition

The rare earth nanomaterials employed in this thesis exhibit tunable emissions in both the visible / NIR and SWIR ranges. They consist of core-shell structures, where the core is composed of NaYF₄ doped with erbium (Er³⁺) as the radiative emitting ion and ytterbium (Yb³⁺) as the sensitizer ion, with a shell of undoped NaYF₄ (Figure 5) [21,28-31].

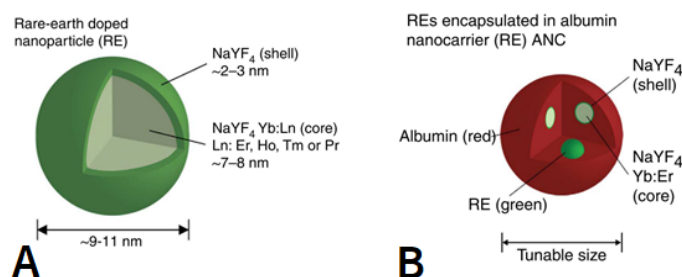


Figure 5: (A) Rare earth nanoparticle structure showing lanthanide- and Yb³⁺-doped NaYF₄ core with undoped NaYF₄ shell. (B) ReANC structure demonstrating albumin encapsulation of the rare earth nanoparticles. Reproduced from [21] with permission from Springer Nature.

NaYF₄ is one of several halide hosts which serve to minimize energy loss by having low vibrational energies [28]. Using NaYF₄, the material loses less energy, leading to higher intensity emissions. Yb³⁺ absorbs light energy maximally at 980 nm and excites from the ²F_{7/2} ground state to the higher energy ²F_{5/2} state [28]. Yb³⁺ can relax back down to the ground state by transferring energy to excite the lanthanide co-dopant to a higher energy level [28]. The emission wavelength thus depends on the exact rare earth

co-dopant used, allowing for tunability. Four rare earths have been investigated previously—Erbium (Er), Holmium (Ho), Thulium (Th), and Praseodymium (Pr)—and each has unique energy states that determine the emission wavelength of the probe (Figure 6) [21]. The focus of this study is on Er-doped ReANCs as doping with Er^{3+} yields the greatest emission efficiency [28].

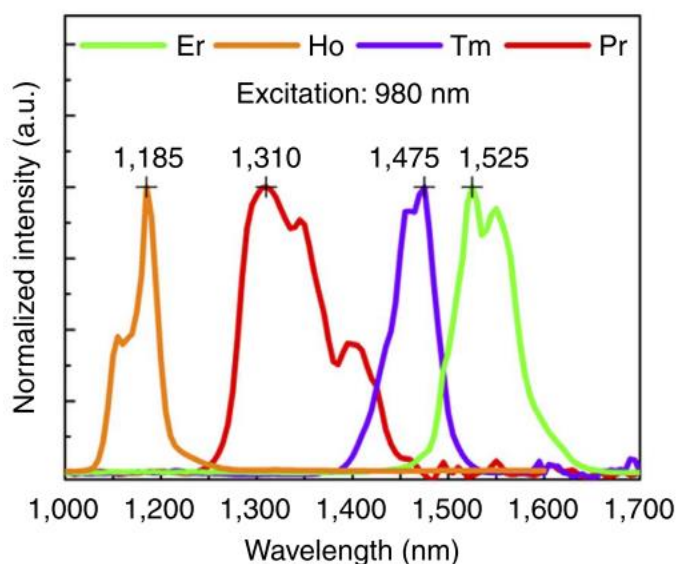


Figure 6: Emission spectra for differently-doped rare earth nanoparticles yield four distinct peaks. Reproduced from [21] with permission from Springer Nature.

Upon excitation, Er^{3+} most commonly transitions from the $^4\text{I}_{15/2}$ state to the $^4\text{I}_{13/2}$ state, and as it relaxes back to $^4\text{I}_{15/2}$ and emits energy, its emission peak lies at 1525 nm [21,28]. In comparison, Ho^{3+} exciting under the same light most commonly transitions from $^5\text{I}_8$ to the $^5\text{I}_6$ energy level, which sets its peak emission wavelength at 1185 nm [21,28]. Each rare earth offers a different energy transition and so a different range of emission wavelengths; however, for all of them, this range is relatively small leading to the rare earth nanomaterial's distinct peaks [28]. Thus, by varying the rare earth dopant, it

is possible to create several different probes that excite under the same 980 nm illumination source but emit at distinct wavelengths, enabling them to be distinguished from one another. However, because the core-shell structure is cytotoxic, insoluble in aqueous solutions, and unfunctionalized on its own, the rare earth materials have been coated with human serum albumin (HSA) to create the final rare earth albumin nanocomposites (ReANCs) [21,28-31]. HSA makes ReANCs biocompatible, water soluble, and capable of being functionalized with targeting molecules [31].

1.4.2: Advantages

Like QDs, ReANCs have tunable emissions that facilitate multispectral imaging. They are also capable of functionalization, which enables targeting, with Zevon *et al.* functionalizing their erbium-doped ReANCs with AMD3100, the ligand to CXCR4, a marker expressed highly in motile cancer cells [29]. Combined with their tunability and narrow peaks, this gives different ReANCs (eg. Erbium, Holmium, and Thulium) the potential to target and distinguish multiple cancer cell types at once, making them ideal for determining tumor heterogeneity and identifying cancers of different subtypes within the same individual. For breast cancer, common phenotypes include estrogen receptor (ER)+/-, progesterone receptor (PR)+/-, and/or human epidermal growth factor receptor 2 (HER2)+/-. Patients can present with a number of different combinations of these receptor statuses. Using multispectral ReANCs targeted to each of the different receptors, one can track all lesions, even those that would be missed when targeting only one cell phenotype. This is an advantage over SWNTs whose broad peaks limit multispectral imaging. ReANCs also have a size advantage over SWNTs. The probes employed in this

study were derived from two separate batches having diameters around 130 nm and 90 nm, where a diameter around 100 nm is optimally sized to target tumors via the EPR effect [30]. ReANCs offer many benefits over other SWIR-emitting agents and as such are prime candidates for comparison of SWIR-guided resection with NIR and visible light-based surgical techniques.

1.5: Aims

1.5.1: Motivation

Recent work has shown the potential of SWIR-emitting rare earth nanoparticles as diagnostic tools and FGS contrast agents [15]. However, there are no existing commercial FGS imaging systems designed for use in the SWIR range. To this end, development of SWIR-detecting FGS hardware and software is needed. A resulting surgical guidance system capable of visualizing ReANC emissions would potentially aid surgeons in resecting tissue with cleaner margins. To bring such a system to the clinic, a comparison study with NIR-guided and visible light resection would provide valuable insight into necessary modifications and validate the predicted advantages of the SWIR system.

1.5.2: Overview

This thesis describes the development of a prototype surgical guidance system based on ReANC SWIR emissions. It compares the accuracy of surgical resection using a prototype SWIR system versus ICG-guided resection, and resection with visual inspection and palpation, with the goal of directly comparing the SWIR system to current and emerging practices. Chapter 2 covers the hardware and software setup for both the

SWIR and NIR systems, with a focus on real-time feedback capabilities. These setups were employed in Chapter 3 in a phantom study. Agarose fluorescent inclusions containing either ICG, ReANCs, or no contrast agent were embedded in gelatin phantoms and imaged under 793 nm or 980 nm excitation (see Section 3.2 for further information). Gelatin phantoms were selected over silicone due to their higher water content and elasticity, which mimic that of tissue more closely. Inclusions were varied in size, depth, and shape and their scattering and emission intensity compared to determine the detectability of each inclusion type. Then, inclusions were resected using white light, NIR, or SWIR guidance and both the resected inclusion and cavity compared to quantify margin accuracy. Last, a pilot *in vivo* animal experiment was performed to demonstrate the potential of the SWIR FGS system as a small animal imager and its performance in living tissue.

1.6: Hypothesis

Based on Section 1.3, it is hypothesized that imaging of ReANC-containing inclusions will demonstrate better resolution at greater depths than ICG-containing and non-fluorescent inclusions. This is because SWIR light experiences less scattering than NIR light in tissue. In turn, it is expected that the ReANC-containing inclusions will be more accurately resected and with less “tumor” left behind than ICG-containing or non-fluorescent inclusions.

CHAPTER 2: INSTRUMENT DESIGN

The goal of this chapter is to outline the design of SWIR and NIR imaging systems optimized for detecting Er-doped ReANCs and ICG emissions respectively. Different optical filters were tested and selected to maximize SBR at the chosen excitation wavelength. In addition, the effect of illumination intensity and field-of-view on image SBR was evaluated. These data were incorporated into the final hardware for the system, which is run by software capable of real-time overlay for surgical guidance.

2.1: Hardware

2.1.1: SWIR Emission Filters

Table 2: Optical Emission Filters				
Manufacturer	Part Number	Transmission Range	Filter ID	Type
Thorlabs	FL1152-10	1147-1157 nm	1152/10 BP	Bandpass
Semrock	BLP01-980R-25	>980 nm	980 LP	Longpass
Thorlabs	FEL1100	>1100 nm	1100 LP	Longpass
Thorlabs	FELH1350 LP	>1350 nm	1350 LP	Longpass
Thorlabs	FB1550-30	1535-1565 nm	1550/30 BP	Bandpass
Thorlabs	FEL1400	>1400 nm	1400 LP	Longpass
Thorlabs	FB1550-40-1	1530-1570 nm	1550/40 BP	Bandpass
Semrock	FF01-1538/82-25	1497-1579 nm	1538/82 BP	Bandpass

Table 2: Optical filters tested for SBR optimization, listing the manufacturer, part number, transmission range, filter ID, and filter type.

Different optical filters were tested (individually and in combination) to determine the ideal set for imaging the SWIR emission from Erbium-doped rare-earth nanocomposites (Table 2). Using an InGaAs camera (Sensors Unlimited, SU320MX-1.7RT), images of a uniform nanoparticle-laden silicone phantom (1 cm thick, 3.5 cm diameter) were taken under uncollimated 980 nm laser illumination (QPhotonics, QFLD-980-50S). This laser was a single-mode fiber-coupled diode with the fiber tip positioned a

distance of 25 cm from the sample, and the nanoparticles used were uncoated Erbium-doped rare earth nanocomposites (REs) with peak emission intensity at 1,525 nm (Figure 7).

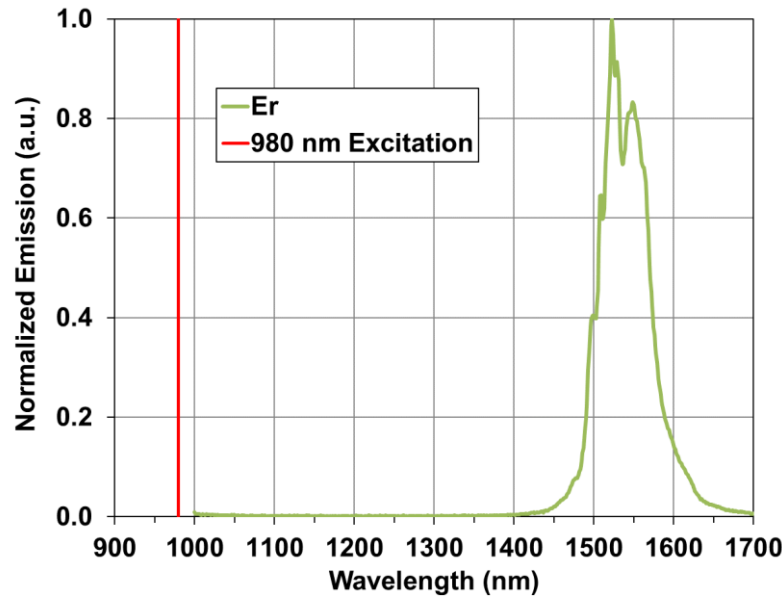


Figure 7: Erbium emission spectrum (green) with 980 nm excitation (red).

This phantom was placed next to a pure silicone control phantom (1 cm thick, 6 cm diameter) such that the laser beam was incident across the interface between the two phantoms (Figure 8). 320x240 pixel images were captured with a frame rate of 15 frames/sec and an exposure time of 16.83 ms using the Sensors Unlimited Image Analysis (SU-IA) Software. 27x27 pixel ROIs were selected from the illuminated sections of the nanoparticle-laden phantom (considered to represent the “signal”), and the control phantom (considered to represent the “background”). Dividing the mean pixel intensity of the “signal” ROI by that of the “background” ROI, the SBR was determined for each emission filter set. The error on the calculated SBR was determined through error propagation of the standard deviations of pixel values in each ROI. In addition to

the emission filters, two different fixed focal length camera lenses were evaluated; a visible-NIR optimized lens (Schneider Optics, Xenon-Topaz f/# 2.0, focal length 38 mm) and a SWIR-optimized lens (Stingray Optics, SR0907-073 f/# 1.4, focal length 25 mm). Images with the VIS-NIR lens were acquired with a 16.83 ms exposure time, while 8.23 ms was used for the SWIR lens.

The filters tested varied in their optical density (OD) and % transmission at the excitation (980 nm) and emission (1525 nm) wavelengths. % transmission (%T) defines the proportion of light passed through a filter, and OD is defined as $OD = -\log_{10}(T)$ where $0 < T < 1$. An ideal filter set has a high %T over the emission range of the contrast agent of interest, indicating that the filter efficiently passes the light over that range. Correspondingly, the OD outside that range, particularly at the excitation wavelength, should be high to prevent scattered illumination light from reaching the detector. Meanwhile, the SBR serves as a measure of tumor distinguishability from healthy tissue and should be maximized by the system. The ideal filter set must therefore allow images of nanoparticle-targeted tissue to be acquired with a high SBR.

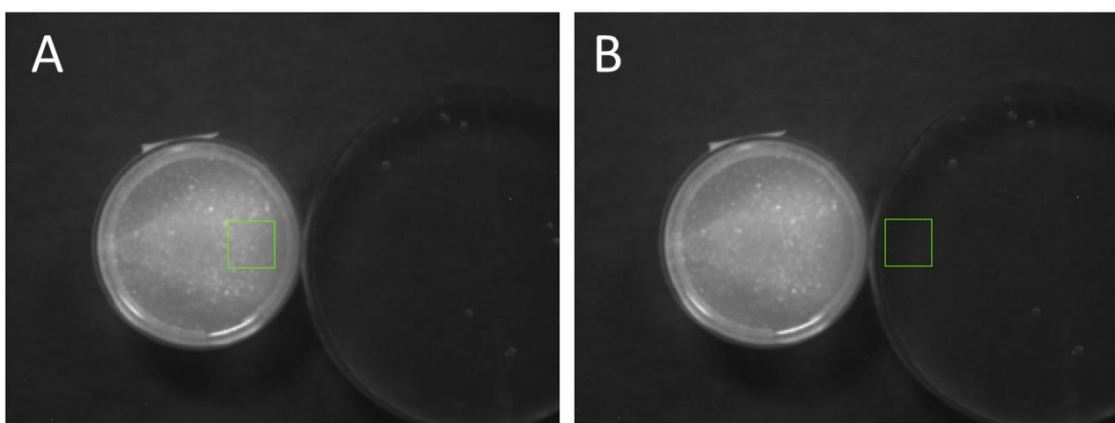


Figure 8: (A) ROI selection of the signal from a nanoparticle-laden phantom and (B) background from a control (nanoparticle-free) phantom using a Xenon-Topaz f/#2.0 lens (Schneider Optics) and BLP01-980R-25 filter (Semrock). The exposure time was 16.83 ms, and the illumination wavelength was 980 nm. Images depict signal values with the laser turned on.

Figure 8 shows the ROI selection process using the Xenon-Topaz f/#2.0 lens (Schneider Optics) and BLP01-980R-25 filter (Semrock). The signal mean pixel value was 2131 while the background mean pixel value was 673, constituting an SBR of 3.17. Figures 9 and 10 show the corresponding data for each filter set and lens evaluated.

For both lenses, the addition of a 1538/82 nm bandpass filter (Semrock) significantly increases the SBR above the SBR values for the other filter sets tested, with the exception of the FB1550-40-1 1550 nm bandpass filter with the Xenon-Topaz lens (Figure 9 and Figure 10). However, this 1550 nm bandpass filter has poor transmission (an average of 19%) for wavelengths within the 1500-1600 nm range. In fact, its transmission band is narrow within this range and peaks at 58% near 1556 nm, implying that it does not collect 1500-1600 nm light as efficiently as the other tested filters. For this reason, it represents a poor choice for imaging. According to the manufacturer's specifications, the 1538/82 nm bandpass filter has a %T of 98% within the 1500 to 1580 nm range and OD 7 at the illumination wavelength of 980 nm. It is therefore excellent at passing the desired emission range while blocking the illumination light, and by coupling it with other filters, the set becomes more adept in this regard. Although addition of other filters decreases transmission at all wavelengths, including the SWIR range, the additional filters block light outside the desired SWIR range more efficiently. For this reason, adding more filters blocks background light to a larger extent than blocking of signal light, improving image SBR despite lowering the overall signal detected.

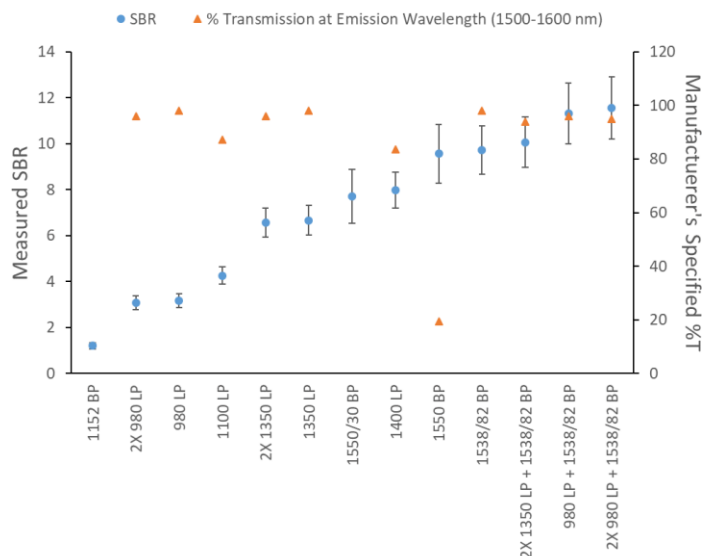


Figure 9: SBR and % Transmission values for different filter combinations (see Table 2 definitions) tested with a VIS-NIR lens. Error bars represent the propagated error of the standard deviations of pixel values in each ROI. All combinations with the 1538/82 bandpass filter have comparable SBR and %T values. Their SBR values are significantly higher than those for filter sets without the 1538/82 nm bandpass filter except for the 1550 nm bandpass filter.

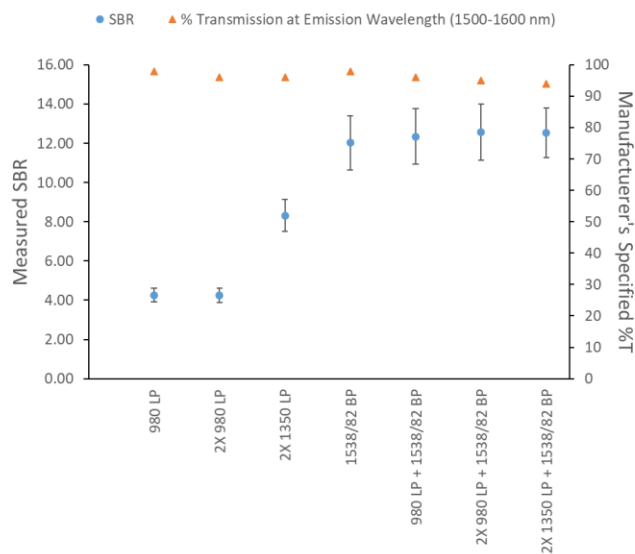


Figure 10: SBR and % Transmission values for different filter combinations (see Table 2 definitions) tested with a SWIR lens. Error bars represent the propagated error of the standard deviations of pixel values in each ROI. All combinations with the 1538/82 bandpass filter have comparable SBR and %T values. Their SBR values are significantly higher than those for filter sets without the 1538/82 nm bandpass filter.

The 980 nm longpass filter (Semrock) and the 1350 nm filter (Thorlabs) have manufacturer's specified %T values of >98% for the ranges 1000-1600 nm and 1350-1700 nm respectively. Their optical density values at 980 nm are OD 7 and OD 5.1, respectively. A combination of the 1538/82 nm bandpass filter (Semrock) with two 980 nm long pass filters results in a theoretical transmission of 95% in the 1500-1600 nm range and OD 21 at 980 nm. Meanwhile, the combined transmission of two 1350 nm longpass filters with the 1538/82 nm bandpass filter is 94% in the 1500-1600 nm range and OD = 17.2 at 980 nm. Both combinations experience a decrease in %T at the emission range and an increase in OD value at the excitation wavelength when the 1538/82 nm bandpass filter is added. This indicates that these combinations are more efficient at blocking the excitation and passing emissions for Erbium ReANCs than any one filter alone. For Erbium-doped nanoparticles, the combination of two 1350 nm longpass filters and one 1538/82 nm bandpass filter was selected for the initial setup of the SWIR imager. In later studies, a combination of two 1064 nm long pass filters (Semrock, BLP01-1064R-25) with the 1538/82 nm bandpass filter was used, yielding a theoretical %T of 86% in the 1500-1600 nm range and OD of 22.7 at 980 nm. While this filter combination is slightly less efficient in theory at transmitting the desired SWIR emissions to the sensor, it is better at blocking contributions from the illumination source.

For the NIR imager, filter sets designed for ICG excitation and emission have been studied extensively and are widely available [36]. The emission filter chosen for ICG imaging was based on ICG's emission spectrum, with the goal of capturing as much fluorescence as possible while minimizing transmission at the excitation laser

wavelength. For this purpose, a 813.5-850.5 nm bandpass filter was selected (Semrock, FF01-832-37-25) (Figure 11).

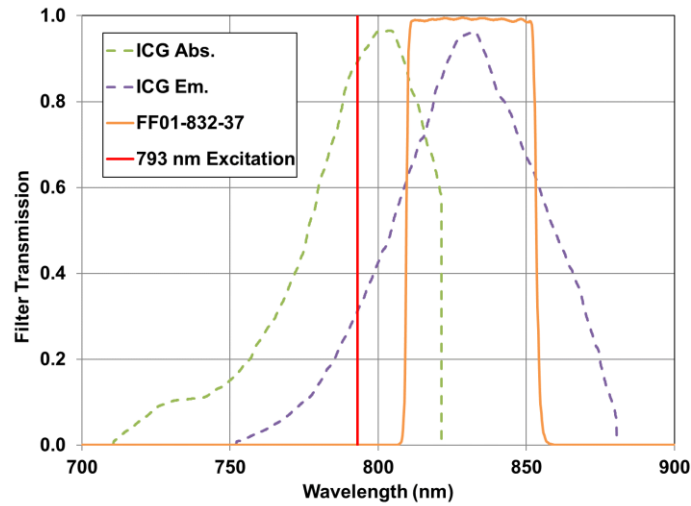


Figure 11: Filter Transmission values for the FF01-832-37 bandpass filter (Semrock) in comparison to the absorption and emission spectra of ICG. The FF01-832-37 best maximizes the transmission of light around ICG's peak emission wavelength (840 nm) while minimizing transmission at the excitation laser wavelength.

2.1.2: Illumination of Rare Earth Phantoms

In a surgical setting, the excitation beam should uniformly illuminate the area on which the surgeon is working. Commercial imagers use beam areas that can be adjusted according to the size of the region of interest. For a smaller surgical area, it may be appropriate to use a smaller beam diameter, in the range of 0.785 cm^2 to 3.14 cm^2 for small tumor resection [17]. In contrast, when imaging a larger area, it is more appropriate to adjust the beam towards a higher FOV, on the order of 200 cm^2 to 300 cm^2 for commercial imagers [7].

The covered area must also have high enough intensity within the safe exposure levels defined by ANSI z136.1 to achieve high SBR within the imaged ROI. To achieve suitable illumination intensity for *in vivo* imaging, previous studies by our research group

have employed a 1 cm diameter (0.785 cm^2 area) collimated beam operating with a power of 1.7 W and an intensity of 2.2 W/cm^2 [21,29-30]. Because the beam area was smaller than the area to be imaged, the illumination source had to be scanned across the subject to build up a fluorescent image. In a surgical setting, it would be impractical to scan the subject while operating, so a series of experiments were run to determine whether imaging could be performed under stationary, wide-field illumination.

For an uncollimated beam diverging from the output of an optical fiber, the area illuminated varies with distance from the specimen, so the effect of illumination source distance from the object on the field of illumination and illumination intensity was evaluated. A nanoparticle-laden phantom (12.5 cm by 12.5 cm by 1.3 cm) was illuminated with the beam diverging from the output of a single-mode fiber-coupled 980 nm diode laser (QPhotonics, QFLD-980-50S), with an output power of 10.4 mW placed at eleven different distances from the phantom. Images were captured with an exposure time of 8.23 ms by the InGaAs camera (Sensors Unlimited, SU320MX-1.7RT) equipped with the SWIR-optimized lens (Stingray Optics, SR0907-073) plus two 1350 nm long pass filters and one 1538/82 nm bandpass filter. Ten images were taken per sample, and using the Sensors Unlimited Image Analysis Software, the beam diameter and mean pixel intensity were measured. To determine the background intensity, images of the 1 cm thick control phantom (Section 2.1.1) were taken and analyzed under identical conditions. The SBR was determined by dividing the mean pixel intensity from the Erbium-doped phantom by the background intensity at each distance.

As a beam propagates from the tip of a single-mode fiber, it diverges and spreads its power out over a wider area with increasing distance from the fiber tip. The beam area is described by the equation:

$$A = \pi \left(\tan \left(\sin^{-1} \left(\frac{NA}{n} \right) d_{eff} \right) \right)^2$$

where NA is the numerical aperture of the fiber (0.14), n is the refractive index of the medium (1 for air), d_{eff} is the effective distance between laser and object, and A is the beam area. According to this equation, it is expected that with increasing distance between laser and object, the area of illumination should increase proportionally to the square of the distance. As the area increases, the intensity is expected to decrease according to the equation $I = P/A$, where P is the fixed output laser power (10.4 mW) and I is the intensity (mW/cm²) over the illuminated area, A . This was the trend observed in the distance tests, where the area of illumination increased with increasing distance from the sample. At the largest distance from the object, 43.0 cm, the beam area was 116.1 cm², approximately the total area of the phantom.

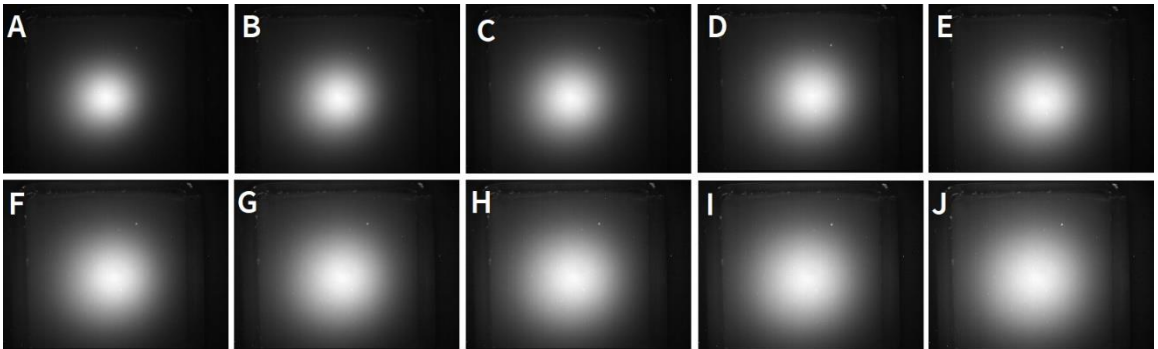


Figure 12: Field of illumination for an Erbium nanoparticle-laden phantom with varying distance between laser and sample demonstrates an increase in illumination area with distance from the sample. (A) Distance 24.91 cm, Diameter 7.04 cm; (B) Distance 27.20 cm, Diameter 7.69 cm; (C) Distance 29.54 cm, Diameter 8.35 cm; (D) Distance 31.89 cm, Diameter 9.02 cm; (E) Distance 32.78 cm, Diameter 9.27 cm; (F) Distance 35.10 cm, Diameter 9.93 cm; (G) Distance 37.44 cm, Diameter 10.59 cm; (H) Distance 38.36 cm, Diameter 10.85 cm; (I) Distance 40.67 cm, Diameter 11.50 cm; (J) Distance 43.00 cm, Diameter 12.16 cm. Images captured were 12-bit.

As expected, the mean pixel value decreased with increasing area of illumination.

The mean background intensity was steady at 77.85 ± 10.86 while the signal intensity decreased nonlinearly with an increase in illuminated area. This experiment characterized the tradeoff between wide field of view and emission signal strength.

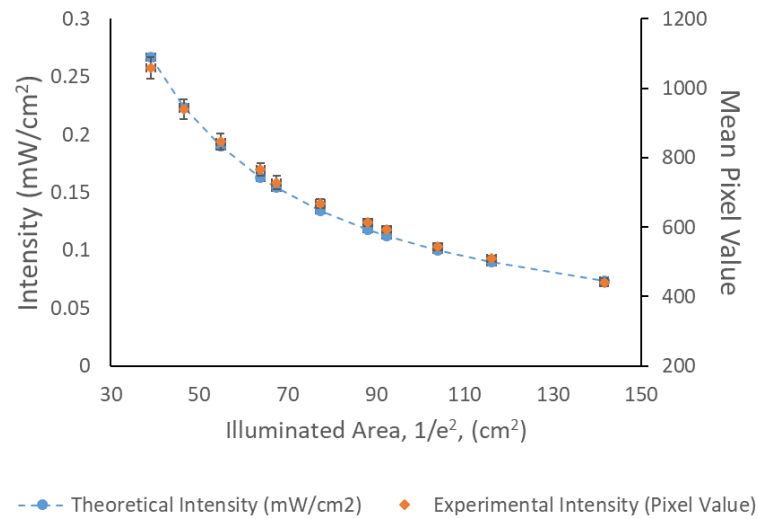


Figure 13: Experimentally-measured average pixel intensity decreases with area illuminated in agreement with theoretically-predicted values according to the relationship $I = P/A$. Data were generated from 12-bit images.

2.1.3: Illumination of ReANC and ICG Phantoms

For safety and biocompatibility, rare earth nanoparticles must be coated in an albumin shell prior to administration to form ReANCs, so it is necessary to optimize the SWIR imaging system for ReANC illumination. To this end, agarose phantoms

containing ReANCs were developed (see Section 3.2). The albumin coat attenuates the measured signal from ReANC emissions such that the SWIR intensity is lower from Er-doped ReANCs than from the naked Er nanoparticles explored in Section 2.1.2. Under the wide field illumination described in Section 2.1.2, the beam intensity is insufficient to achieve a measurable signal from ReANCs at a concentration typical of *in vivo* work. Instead, a higher power illumination source is needed.

To illuminate the ReANC-containing phantoms, a multimode fiber coupled diode laser (Opto Engine LLC, MDL-H-980nm-5W) with a output power of 1.8 W was used. The beam was collimated with a 36 mm focal length collimator (Thorlabs, F810FC-780) for a final illumination area of 0.785 cm². This collimation maintains a constant beam area and keeps the illumination intensity high to achieve a strong signal. However, because the beam area was too small to cover the entire ROI, the laser was scanned manually across each phantom to create a uniform coverage of the area.

For comparison, phantoms containing ICG were similarly fabricated and imaged. To illuminate the ICG-containing phantoms, a 785 nm laser (Opto Engine LLC, MDL-III-785nm-2.5W) with an output power of 2500 mW was used. This is comparable in wavelength and power to many commercial imagers and would allow for future imaging with IReDye800, which excites at a similar range [7,18]. The beam was collimated in the same manner as with the ReANC-containing phantoms and scanned from the same distance from the object so that the area of illumination was equivalent between contrast agents.

2.1.4: Final Design

The final SWIR imaging setup (Figure 14) contains an InGaAs camera (Sensors Unlimited, SU640HSX-1.7 RT) with a 25 mm focal length lens (StingRay Optics, SR0907-073). The camera captures 12-bit, 640x512 pixel images with an exposure time of 32.98 ms at a frame rate of 33.3 fps. The digital gain for the ReANC experiments outlined in Chapter 3 was 1.25. The camera is equipped with one 1538/82 nm bandpass filter (Semrock) and two 1064 nm long pass filters (Semrock) and mounted 35 cm from the object. A 5W diode laser (Opto Engine LLC, MDL-H-980nm-5W) coupled to a 400 μm diameter multimode fiber with a 36 mm focal length collimator (Thorlabs, F810FC-780) illuminates the specimens with a power of 1.8 W.

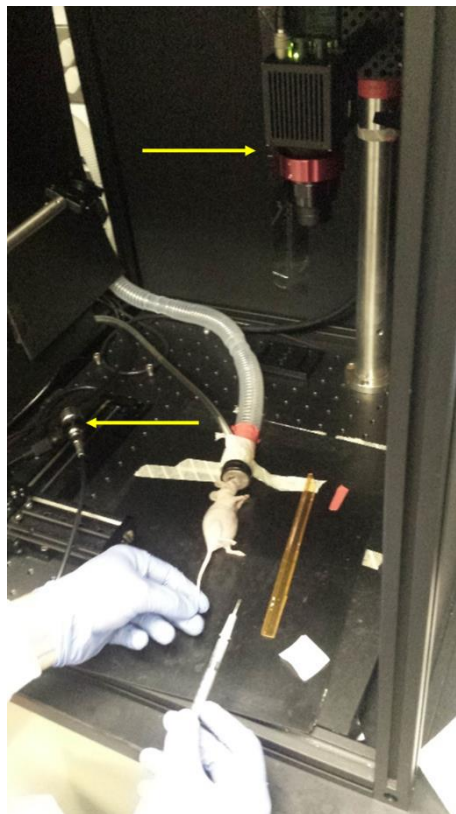


Figure 14: Final setup for SWIR imaging consisting of a collimated 980 nm laser for illumination and an InGaAs SWIR-detecting camera equipped with a lens and filters for detection. Arrows indicate the position of the camera and illumination source.

The final NIR imaging setup employs the Zyla 5.5 sCMOS camera (Andor) operating with a 38 mm focal length lens (Schneider Optics). The camera captures 12-bit, 2048x2048 pixel images and exposure time of 1 ms. The camera is equipped with an 832/37 nm bandpass filter (Semrock), capable of transmitting light in the range of 813.5 nm to 850.5 nm (Figure 11). For the ICG experiments outlined in Chapter 3, a 2.5 W 785 nm laser (Opto Engine LLC, MDL-III-785nm-2.5W) fiber-coupled to a 36 mm focal length collimator (Thorlabs, F810SMA-780), 400 μ m diameter fiber, and 795-805 nm bandpass filter (Thorlabs, FB800-10) illuminates specimens with output current 380 mA and power 12 mW. Coupling of the illumination source to the bandpass filter centers the illumination peak at 793 nm and eliminates long wavelength emissions from the laser that can be transmitted by the emission filter at the camera (Figure 15). The 795-805 nm filter was tilted slightly to shift its transmission band to shorter wavelengths, closer to the peak of the laser emission.

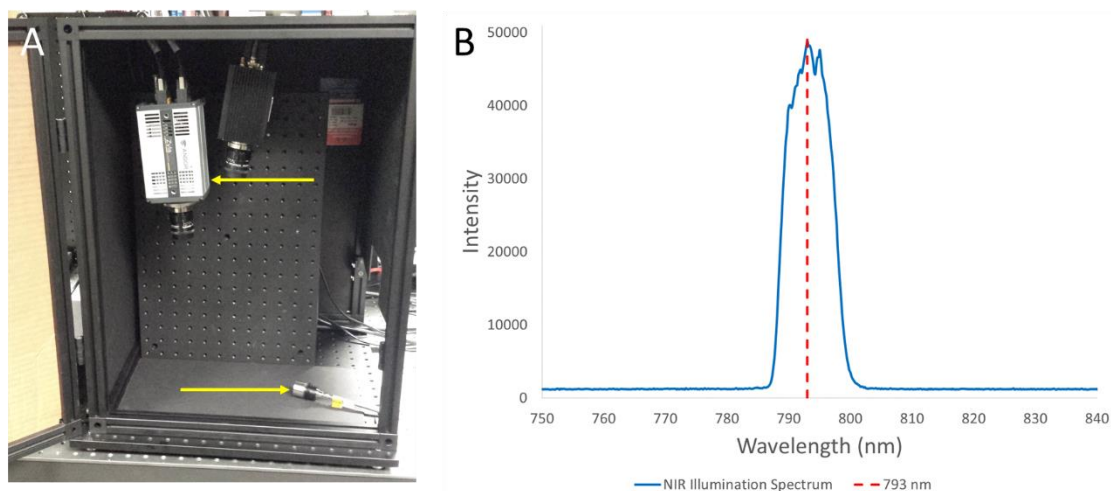


Figure 15: (A) Final setup for NIR imaging consisting of a collimated 785 nm laser for illumination and an sCMOS NIR-detecting camera equipped with a lens and filters for detection. Arrows indicate the position of the camera and illumination source. (B) The illumination spectrum of the NIR laser is centered at 793 nm when equipped with a tilted 800 nm bandpass filter (Thorlabs, FB800-10).

Table 3: Experimental Parameters for ICG and ReANC Imaging Setups		
	ICG imaging	Erbium ReANC imaging
Excitation wavelength	793 nm	980 nm
Excitation power	0.012 W	1.8 W
Illumination area	0.79 cm ²	0.79 cm ²
Illumination intensity	0.015 W/cm ²	2.28 W/cm ²
Spectral collection band	814 – 851 nm	1497 – 1579 nm
Camera model	Andor Zyla 5.5 sCMOS (silicon)	SU640HSX (InGaAs)
Camera pixel size	6.5 mm	25 mm
Camera pixel count	2560 x 2160	640 x 512
Camera pixel binning	1x1	N/A
Camera quantum efficiency	25%	80%
Camera noise	1.2 e- (read noise)	35 e- (RMS)
Camera exposure time	1 ms	33 ms
Camera lens f/#	f/2	f/1.4
Fluorophore quantum efficiency	9.3% [37]	1.17% [38]
Fluorophore concentration	0.01 mg/ml	0.60 mg/ml

Table 3: Summary of experimental parameters used for imaging ICG and erbium ReANC based phantoms.

2.2: Software

LabVIEW, a graphical programming interface, is the platform for the proposed imaging system. The imaging software must be able to capture white light and fluorescent images and overlay them in real-time, allow adjustment of the display, and save captured images for post-processing analysis. Since the illumination beam is scanned across the specimen, as mentioned in Section 2.1.3, the imaging software must build up a final SWIR image by combining the SWIR signals from each captured frame.

The SWIR image alone indicates areas of interest where the contrast agent is concentrated but fails to capture anatomical features. Consequently, it is helpful to overlay the SWIR image in real-time on a white light image to provide anatomical context during a surgical procedure.

The imaging display is shown in Figure 16. A panel on the left-hand side of the screen contains all the controls for operation, and the user may input the file and folder names for the white light, fluorescent, and overlay images to be saved before starting a procedure. Upon initiating a run, the program automatically interfaces with the camera and captures an image of the field of view under white light illumination. This image is displayed in the lower right of the screen. A real-time running image is featured in the top left of the screen, and the user is allowed time to adjust the illumination and display settings for fluorescence imaging before beginning the overlay. By pressing the “Start Overlay” button, the user prompts the program to build up a maximum intensity image, constituting the SWIR image displayed on the top right of the screen. If the “Enable Overlay” switch is on, then a real-time overlay of the SWIR image on the white light image appears in the bottom left of the screen. If this switch is off, then no overlay occurs. The transparency of the SWIR image in the overlay can be adjusted via a slider in the left-hand control panel, where 0% makes the SWIR image completely opaque and 100% makes it completely transparent. The default transparency is 50%. The user can likewise adjust the brightness of the white light image during overlay using a similar slider, where 0% is dark and 100% is bright. In this way, better contrast between the SWIR and white light images in the overlay may be achieved.

For *in vivo* work, the emission intensity may be too low to see during the run, so the program also offers the ability to scale the display intensity of the running, SWIR, and overlay images, allowing the user to select a custom minimum and maximum pixel intensity value. By selecting a lower maximum, the user increases the display brightness of low intensity signals. By selecting a higher minimum, the user can effectively set a threshold to only display pixels with values above the noise floor. This display scaling can be switched on and off using the “Scale Intensity of Max Image” button. Once the user has finished their work, they may press the “Stop Overlay” button to end the program and save copies of the unscaled SWIR images as 16-bit .tif files with pixel values stored in the 12-bit (0-4095) range. The white light and overlay images are saved as .tif files with the original 12-bit pixel values (0-4095) linearly mapped to values between 32768 and 36863 for 16-bit storage. 8-bit versions of these white light and overlay images are also saved for display purposes. All images were 512x640 pixels. Saved images are grayscale, and the displayed images are colormapped to the “Temperature” palette, which ranges from black to red to white.

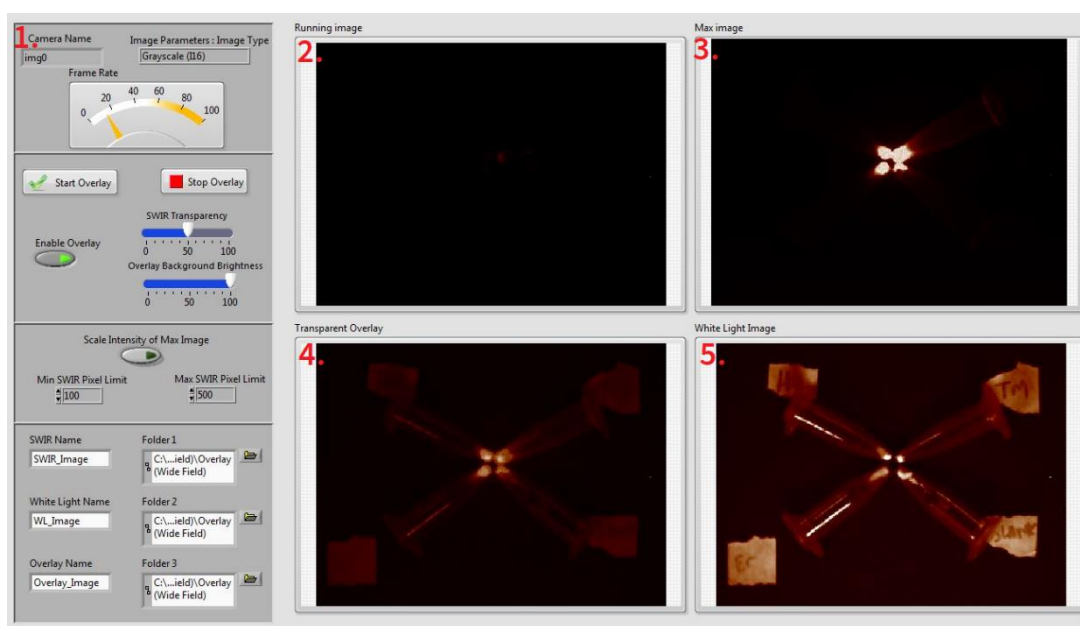


Figure 16: Software display screen showing: (1) a control panel, (2) The running image, (3) the fluorescent image, (4) the real-time overlay, and (5) the white light image.

For NIR imaging, a separate LabVIEW interface was developed using the Andor Software Development Kit (SDK) to interface with the Zyla 5.5 camera, offering the same features as with the previously-described SWIR software. As an additional step, the NIR images were captured as 2048x2048 images and scaled down to 1000x1000 to make the images small enough for real-time processing.

CHAPTER 3: PHANTOM STUDY

This chapter aims to draw direct comparisons between the FDA-approved NIR imaging agent ICG and novel SWIR-emitting ReANCs through a controlled phantom study. It has been previously shown that tissue-mimicking phantoms can be used to simulate fluorescence imaging in a surgical setting [20]. In particular, Pleijhuis *et al.* employed a phantom study to evaluate the efficacy of ICG as a tumor imaging agent in breast-conserving surgery [20]. In their work, ICG-containing agarose inclusions, which simulated probe-targeted tumors, were embedded in a gelatin phantom that mimicked the optical properties of healthy tissue [20]. Upon imaging and resection of these phantoms, Pleijhuis *et al.* determined that ICG is a promising imaging agent for improving margin accuracy in surgical resection of tumors [20]. The goal of the following experiments is to adapt the protocol outlined by Pleijhuis *et al.* in the assessment of Er-doped ReANCs as FGS imaging agents. By comparing ReANC guidance directly to ICG guidance, it may be possible to determine the practicality and potential benefits to using ReANCs as fluorescent probes in tumor resection.

3.1: ReANC Synthesis

Controlled coacervation was used to synthesize the ReANCs according to the protocol outlined by Naczynski *et al.* [21]. A solution of 0.2 mg/mL of rare earth core-shell structures was prepared in 100% ethanol. In a 10 mM NaCl solution in water, a 20 mg/mL HSA solution was prepared and adjusted to pH 8.5 ± 0.05 . At a drop rate of 1.5 mL/min, 2 mL of the rare earth solution was added to 0.5 mL HSA via a syringe pump. The solution was kept under constant stirring at a rate of 1000 rpm during the addition of

rare earths. Then, 2.34 μL of glutaraldehyde was added to the final solution to cross-link the albumin shell. The solution was left to stir at 1000 rpm for 16-18 hrs, producing an end total of seven vials per batch. After, the vials were divided into four tubes and centrifuged at 48,400 g for 10 min at 4 C. The supernatant was removed, and the pellets were resuspended in 3.5 mL PBS and centrifuged again. After removal of the supernatant, the pellets were resuspended in 3.5 mL PBS again, and the four tubes were combined into two tubes to double the effective end concentration of rare earths. The tubes were centrifuged a final time and resuspended in 350 μL for a final concentration of ReANCs of 4 mg/mL (20x greater than the initial RE core-shell concentration), where 2 mg/mL (10x) is typically administered in a 100 μL volume and 0.6 mg/mL (3x) is the estimated concentration of ReANCs retained at tumor sites during *in vivo* work.

3.2: Agarose-Gelatin Phantoms

3.2.1: Rationale

While silicone is commonly used as a host matrix for tissue simulating phantoms, this material has low water content. Agarose and gelatin-based phantoms are water-based and therefore should mimic better the absorption properties of tissue in the SWIR region, where water is known to exhibit distinct absorption features. Moreover, silicone phantoms are stiff and difficult to cut with surgical tools while agarose and gelatin-based phantoms have elastic properties similar to that of tissue [20]. Agarose and gelatin can be cut with surgical instrumentation and thus allow for comparisons between fluorescence-guided and palpation-guided resection [20].

3.2.2: Fabrication

Phantoms were synthesized according to the protocol outlined by Pleijhuis *et al.* [20]. In brief, agarose inclusions containing the contrast agent of interest were placed at known depths within a surrounding gelatin matrix. To create the inclusions, a solution of 1x tris buffered saline (TBS) was first prepared by diluting one part 10x TBS (BioRad) in nine parts deionized (DI) water by volume. Sodium azide (Fisher Scientific) was added to this 1x TBS solution to prevent microbial growth, giving a final concentration of 1 mg/mL. Type I agarose (Sigma Aldrich) was added to the 1x TBS in a ratio of 2 g agarose per 50 mL 1x TBS, and the solution was brought to a boil by heating at 120 °C under constant stirring [20]. In a final step, either ICG or Er-doped ReANCs were added to the agarose slurry in a ratio that achieved the final desired concentrations.

For the SWIR inclusions, 4 mg/mL Er-doped ReANCs were sonicated for 20 minutes to resuspend the particles and then added to the agarose mixture for a final concentration of 0.6 mg/mL in the inclusion. For NIR inclusions, a solution of ICG (MP Biomedicals, LLC) in water with concentration 0.239 mg/mL was added to the agarose mixture to achieve a final concentration of 14 μ M [20]. The agarose mixtures were injected into custom designed, 3D-printed PLA molds using a micropipette, covered with aluminum foil, and left to solidify for 30 minutes at room temperature (Figure 17).



Figure 17: 5 mm diameter agarose inclusions containing Er-doped ReANCs, formed in 3D printed molds.

The surrounding gelatin matrix was synthesized in multiple layers to achieve each desired depth. 225 g bloom gelatin from bovine skin (Sigma) was dissolved in 1x TBS in a ratio of 1 g gelatin per 10 mL 1x TBS, and the mixture was heated at 80 °C under constant stirring [20]. Once dissolved, the mixture was cooled to 35 °C, and nigrosin (1.5 mg/L) was added for a final concentration of 0.0075 mg/mL. For scattering, Intralipid 20% was added for a final concentration of 1% Intralipid [20]. For each layer, a volume of the gelatin mixture necessary to achieve a predetermined thickness (inclusion depth) was poured into a prechilled container and allowed to solidify for 30-60 min at 4 °C [20].

Post-solidification, the agarose inclusions were removed from their molds and pinned in place on the gelatin phantom. After pinning, the next gelatin layer was poured on top of the existing layer and allowed to solidify for 30-60 min at 4 °C. This layering process was repeated until all the inclusions were incorporated. The final phantom solidified overnight at 4 °C, and its container was covered with aluminum foil to prevent light exposure. Prior to imaging, the retaining pins were removed from the phantom.

3.3: Chicken Breast Experiments

While the gelatin phantoms described in Section 3.2 were synthesized to mimic the optical properties of tissues, biological tissue is less uniform and laden with inhomogeneities that affect its light attenuation properties. Unlike phantoms, biological tissue also contains extra components like blood, proteins, lipids, and more, which further influence light propagation through it. As the goal of this work is to evaluate the clinical potential of ReANCs, it is necessary to study the attenuation of the SWIR emissions within a representative tissue that incorporates these attenuating features. Using fresh *ex vivo* chicken breast, the attenuation of ReANC emissions through tissue was evaluated. Taking this data into account, it was possible to design the gelatin phantom in a manner that is more characteristic of biological tissue.

Slices of chicken breast were obtained and stored at 4 °C in a conventional freezer. Prior to imaging, slices were cut at varying thicknesses and placed over agarose inclusions containing 0.6 mg/mL of 130 nm diameter Er-doped ReANCs. Using the SWIR system described in Section 2.1.3, 16-bit SWIR images were captured. The fluorescent intensity of the inclusions was evaluated at each thickness to gauge the appropriate range of depths at which to embed the inclusions within the gelatin phantoms (Section 3.4).

In initial experiments, cuts of chicken with thicknesses 1.6 mm, 2.5 mm, and 5 mm were placed over a 5 mm diameter ReANC-containing inclusion and illuminated by under 1.8 W power 980 nm light (Figure 18). ROIs were selected from the fluorescent images at each thickness, with the area of the inclusion constituting the signal and a

second area selected from the illuminated chicken breast serving as the background. Pixel intensity at the site of the inclusion decreased with increasing thickness of the chicken breast, and the signal intensity was nearly at the background level at the 5 mm tissue thickness (Figure 19).

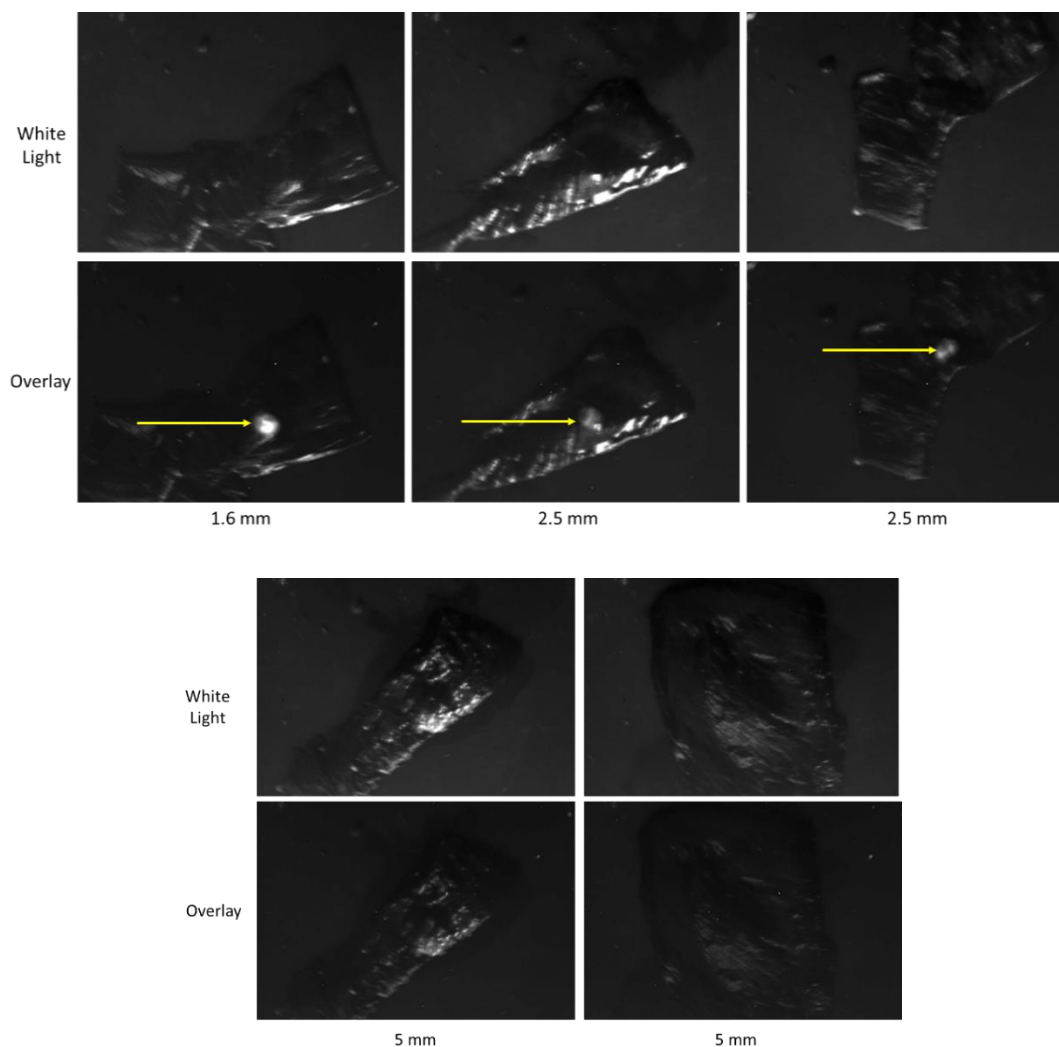


Figure 18: White light (top) and SWIR overlay (bottom) images of a 5 mm diameter agarose inclusion containing an ReANC concentration of 0.6 mg/mL beneath chicken breast of thicknesses 1.6 mm, 2.5 mm, and 5 mm. Yellow arrows point to detected signals from the inclusion. Signal intensity decreased with chicken breast thickness, and at 5 mm, no signal was discernible by visual inspection.

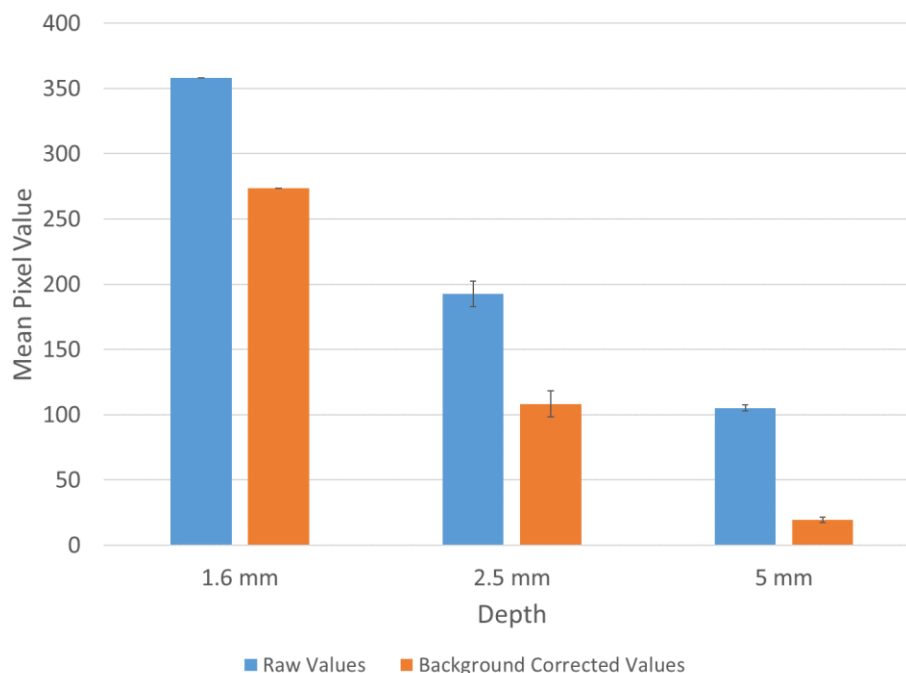


Figure 19: Summary of raw and background-corrected average pixel intensities for 12-bit images of a 5 mm diameter Er ReANC-containing inclusions placed below varying thicknesses of chicken breast. As chicken breast thickness increased, average pixel intensity of the signal decreased.

An identical experiment was repeated with a 5 mm diameter inclusion containing a 0.6 mg/mL concentration of ReANCs and chicken breast slices of thicknesses 1 mm through 8 mm. As before, pixel intensity decreased with increasing chicken breast thickness. By 5 mm thickness, the average pixel intensity of the inclusion exceeded background levels by only 9.5 units. At 6 mm thickness, the difference in pixel intensity between signal and background was so marginal that the SBR dropped to 1.

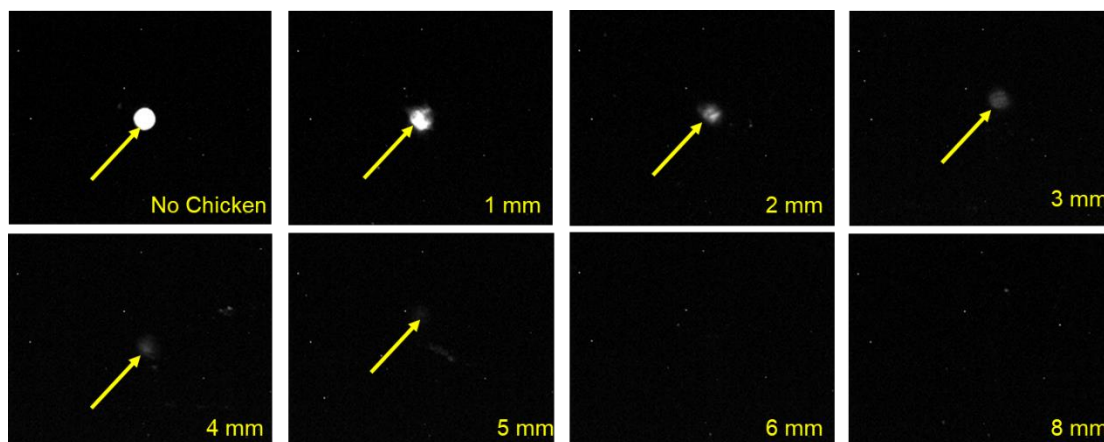


Figure 20: SWIR images of a 5 mm diameter agarose inclusion containing an ReANC concentration of 0.6 mg/mL below chicken breast of thicknesses 1 mm, 2 mm, 3 mm, 4 mm, 5 mm, 6 mm, and 8 mm. Yellow arrows point to detected signals from the inclusion. Signal intensity decreased with chicken breast thickness, and at 6 mm, no signal was discernible by visual inspection.

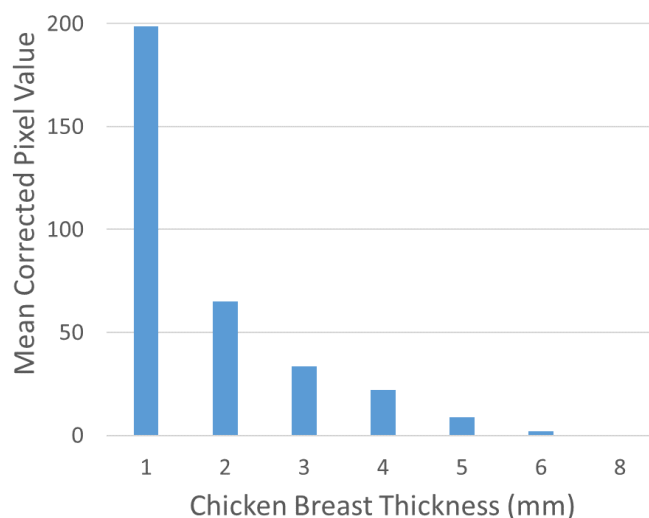


Figure 21: Summary background-corrected average pixel intensities for 12-bit images of a 5 mm diameter Er-doped ReANC-containing inclusions placed below varying thicknesses of chicken breast. As chicken breast thickness increased, average pixel intensity of the signal decreased and dropped down to background level at 6 mm thickness.

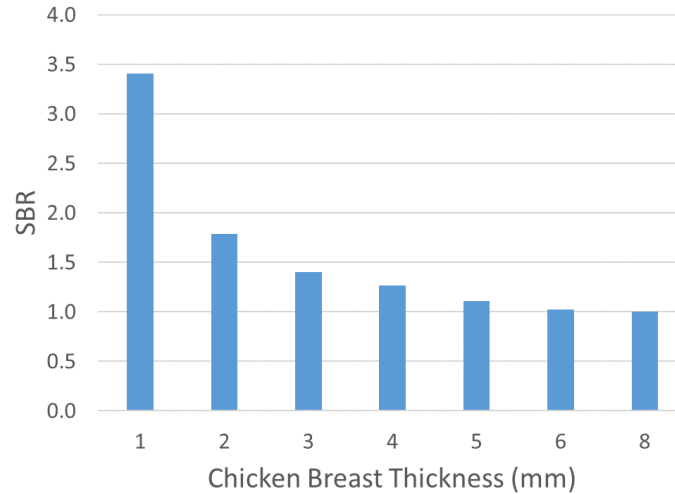


Figure 22: Summary SBR for 12-bit images of a 5 mm diameter Er ReANC-containing inclusions placed below varying thicknesses of chicken breast. As chicken breast thickness increased, SBR of the signal decreased and dropped down to 1 at 6 mm thickness.

3.4: Inclusion Size and Depth Experiments

Solid tumors can be small, making them difficult to detect and remove, and in FGS, the size of the lesion influences the intensity of its emissions. The amount of fluorescent probes retained by a lesion varies with lesion size. With more probes, there is a higher number of excitation and emission events, leading to a stronger detected signal; however, detection is still limited by lesion depth. At large subsurface depths, a fluorescent signal must travel farther through the tissue and is more attenuated by scattering and absorption events. An FGS system suited for deep tissue imaging must be capable of detecting solid tumors within a range of biologically-relevant sizes and depths. Here, the effect of inclusion size and depth on detectability for the proposed system have been evaluated with the goal of determining the limiting detection depth for a fixed size inclusion.

3.4.1: Phantom Design

Based on the data from the chicken breast studies (Section 3.3), 5 mm is the limiting depth past which no signal from a 5 mm diameter ReANC-containing agarose inclusion of the selected concentration will be detected. For the size-depth phantom studies, agarose inclusions of three diameters sizes—5 mm, 7.5 mm, and 10 mm—were placed in a gelatin phantom at three different depths—1 mm, 3 mm, and 5 mm. The layout of this phantom is that seen in Figure 23.

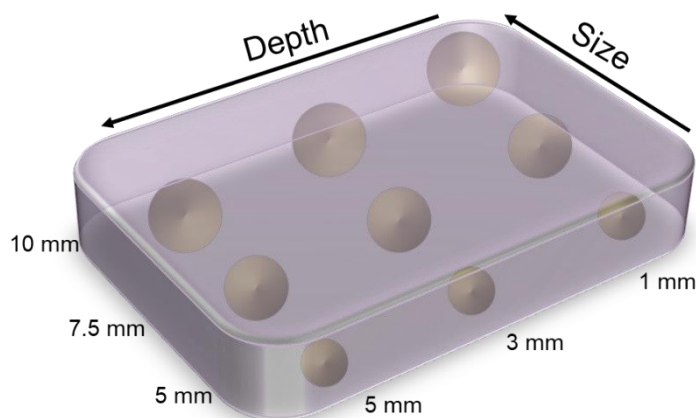


Figure 23: Design of size-depth testing phantom showing agarose inclusions of 5 mm, 7.5 mm, and 10 mm diameters placed at depths between 1 mm and 5 mm within a gelatin phantom. One corner is notched to determine orientation upon imaging.

3.4.2: Methods

Agarose inclusions containing 91 nm ReANCs were embedded in a gelatin phantom according to the protocol outlined in Section 3.2.2 and following the design from Figure 23.

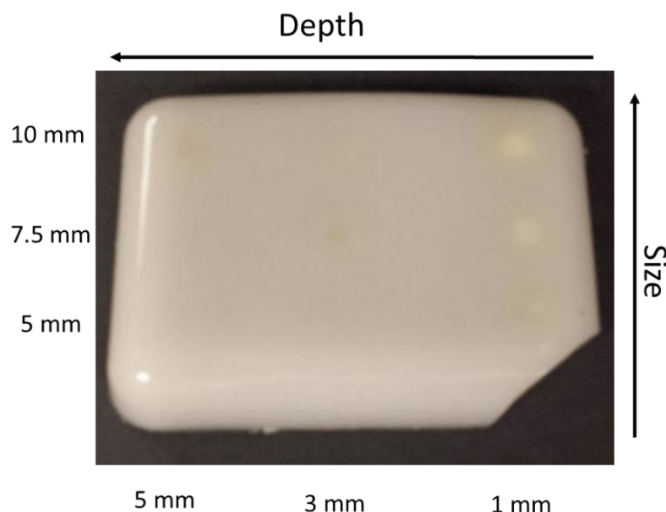


Figure 24: Size-depth phantom containing 0.6 mg/mL ReANC agarose inclusions of 5 mm, 7.5 mm, and 10 mm diameter embedded at depths of 1 mm, 3 mm, and 5 mm. The notched corner indicates orientation.

Using the SWIR imaging setup (Section 2.1.4) and imaging software (Section 2.2), white light images were obtained under illumination with an infrared heat lamp. A 980 nm collimated beam with a power of 1.8 W and beam area of 0.785 cm^2 was manually scanned across the phantom to build up the fluorescent and overlay images in real-time. Six independent scans were performed for two different orientations of the phantom for a total of twelve images. For each, a circular ROI was selected around the detected signals in the fluorescent image using ImageJ, and a background ROI was taken from a region of the phantom without any inclusion embedded. Background-corrected mean pixel values were determined by subtracting the background mean pixel value from the inclusion mean pixel value for each inclusion.

3.4.3: Imaging Results

ReANCs-containing inclusions of all three diameters were detected at the 1 mm and 3 mm depths, while no signal was detectable from any size inclusion at the 5 mm depth (Figure 25).

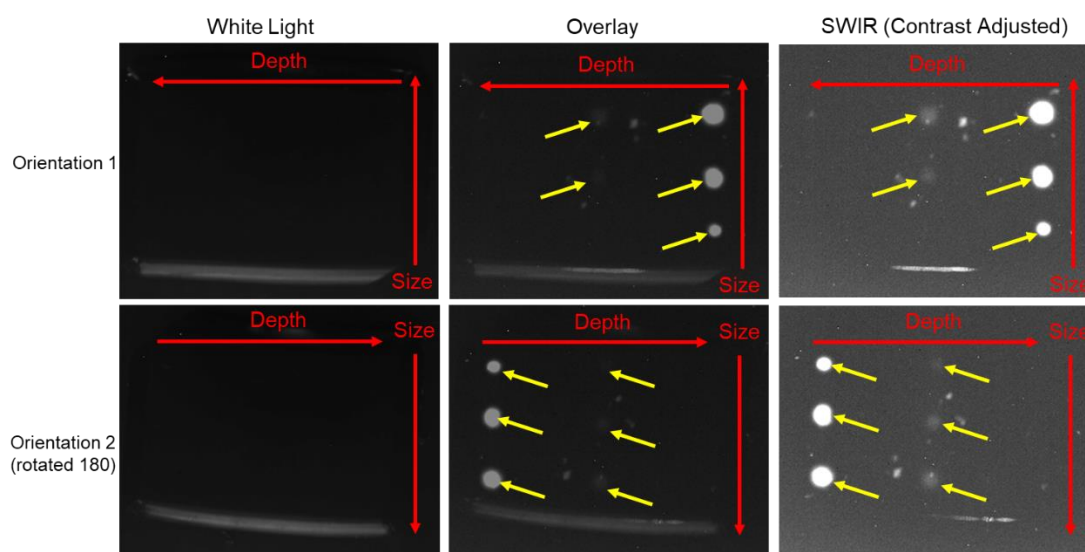


Figure 25: White light, SWIR overlay, and contrast adjusted SWIR images of a size-depth phantom containing 0.6 mg/mL ReANC agarose inclusions of 5 mm, 7.5 mm, and 10 mm diameter embedded at depths of 1 mm, 3 mm, and 5 mm. The phantom was imaged at two orientations (0 and 180 degree rotations) to take into account variations in scanning illumination. The SWIR image contrast was enhanced to better visualize the 3 mm deep signals. Red arrows indicate progression of inclusion depth and size. Yellow arrows indicate regions of fluorescent signal intensity. The raw SWIR image had a range of pixel values between 0 and 4095, and the contrast adjusted SWIR image was scaled between values 40 and 500 for display only.

In the 0 degree rotation orientation, mean pixel values decreased with decreasing inclusion diameter for both 1 mm and 3 mm depths. This trend was observed also in the 180 degree rotation except that the 10 mm diameter inclusion had a lower mean pixel value than the 5 mm and 7.5 mm inclusions at 1 mm deep.

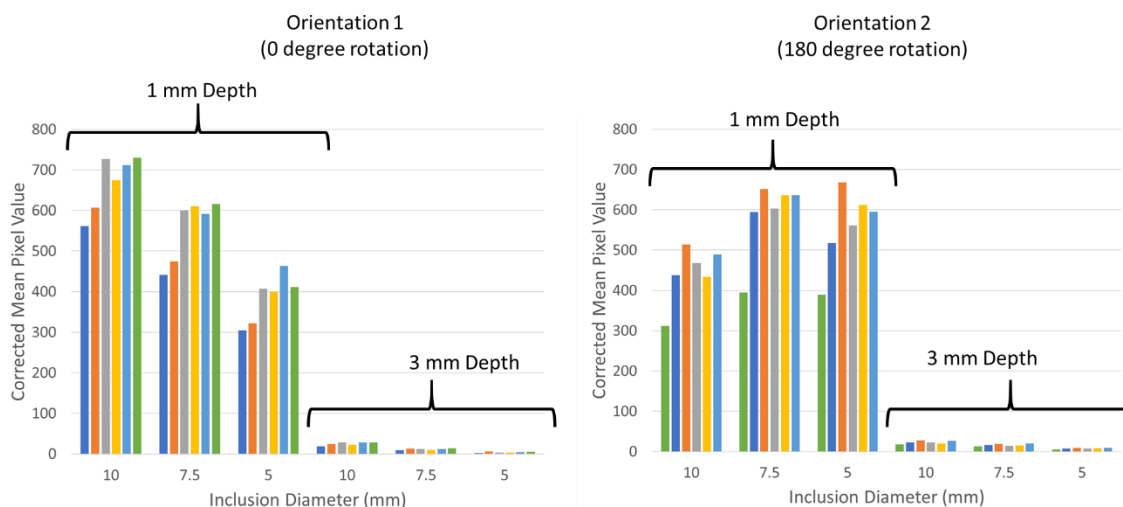


Figure 26: Background corrected mean pixel values for 5 mm, 7.5 mm, and 10 mm diameter 0.6 mg/mL ReANC agarose inclusions at 1 mm and 3 mm depths into a gelatin phantom. Different color bars indicate different scans of the same phantom. Values represent the mean pixel value for each inclusion minus the background mean pixel value. For the 0 degree orientation, the mean pixel value decreased with decreasing size. For the 180 degree orientation, a similar trend was observed with the exception of the 10 mm diameter inclusion at 1 mm deep.

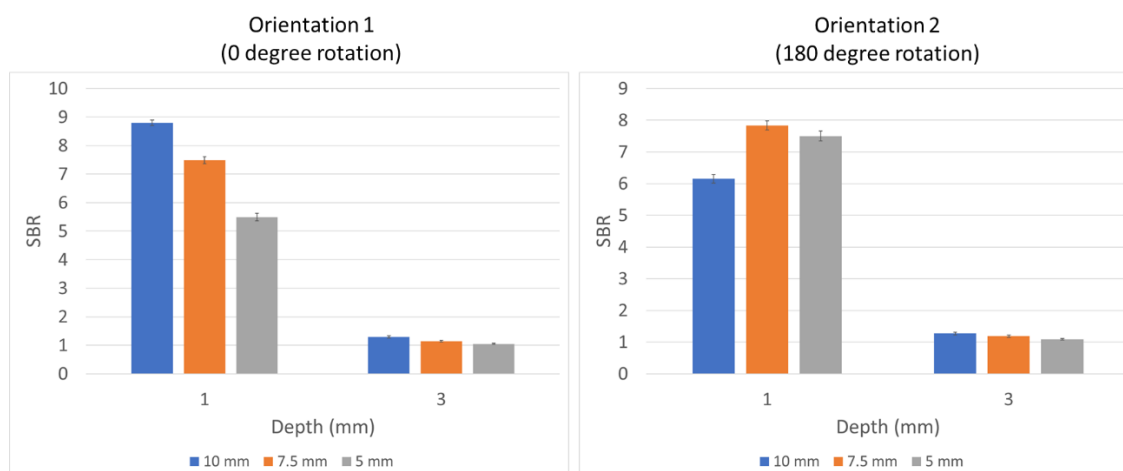


Figure 27: SBR values for 5 mm, 7.5 mm, and 10 mm diameter 0.6 mg/mL ReANC agarose inclusions at 1 mm and 3 mm depths into a gelatin phantom. Values reported are averages of different scans of the same phantom in the same orientation. Error bars represent the standard deviation between different scans. SBR approaches 1 at 3 mm deep for all three sized diameters, indicating a 3 mm limiting depth.

For both orientations, the SBR dropped to values near 1 at the 3 mm depth for all inclusions, indicating a 3 mm limiting depth for ReANCs within the phantom.

To determine whether the difference in trends between the two phantom orientations was due to nonuniform illumination, the uniform nanoparticle-laden silicone phantom (12.5 cm by 12.5 cm by 1.3 cm) described in Section 2.1.2 was scanned and imaged under 980 nm at 0.026 W power. ROIs selected around the phantom, each corner, and the center were evaluated for their mean pixel values. For the whole phantom ROI, a histogram was calculated to determine the pixel distribution.

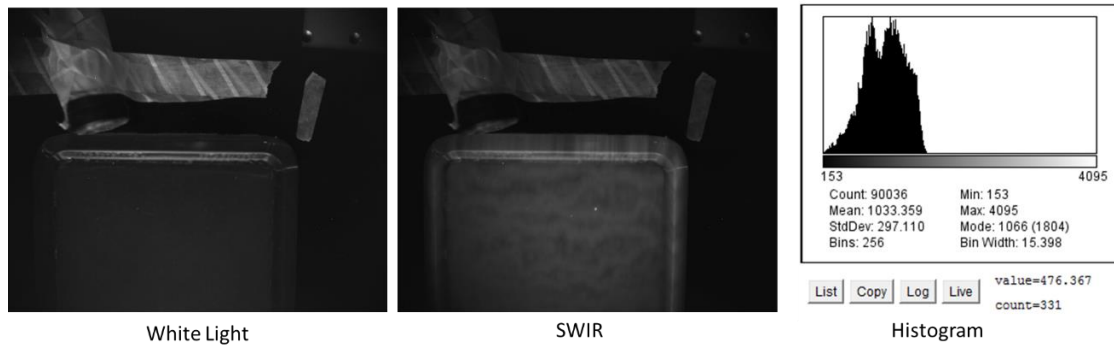


Figure 28: White light and SWIR images of a uniform nanoparticle-laden phantom scanned with a 0.026 W 980 nm collimated laser and the accompanying histogram of the whole phantom ROI. The %CV for the pixel values across the region was 28%, indicating a significant variation in the illumination intensity.

Table 4: Average Pixel Values of a Uniform Phantom	
ID	Mean
Whole Phantom	1074
Lower Left Corner	583
Upper Left Corner	937
Upper Right Corner	1297
Lower Right Corner	854
Center	1323

Table 4: Mean pixel values for different regions of a uniform nanoparticle-laden phantom imaged under 0.026 W 980 nm collimated laser light. The lower left corner demonstrates decreased illumination intensity compared to the other illuminated regions.

The whole phantom histogram demonstrates a coefficient of variation (%CV) in pixel values of 28%, suggesting a significant variation in illumination during the scan. Referring to the measured mean pixel values, this variation can be attributed to the decrease in illumination when scanning the lower left-hand corner of the phantom. There, the mean pixel value dropped by half compared to other regions within the field of illumination. When the phantom was positioned in the second orientation, the 10 mm diameter inclusion placed 1 mm deep was placed in the lower left-hand corner where the illumination intensity was likely lower compared to the rest of the phantom. This may account for the lower mean pixel value seen for this inclusion compared to the inclusions of smaller diameter.

3.5: Inclusion Scattering and Resolution Experiments

SWIR wavelengths scatter less through biological tissue than do NIR wavelengths, and the cumulative effects of scattering increases with the thickness of tissue through which light must pass. This scattering not only attenuates the signal but can blur the appearance of the detected image. In a surgical setting, scattering must be minimized to ensure signal detection and high resolution at greater depths, as well as an accurate measure of tumor boundary geometry. A quantitative study on the effect of tissue depth on scattering has been performed to (1) determine the level of scattering of ICG-tagged and ReANC-tagged inclusions at varying depths and (2) evaluate the impact of such scattering on resection accuracy.

3.5.1: Phantom Design

Based on the results from the size-depth phantom experiment (Section 3.4), the strongest detected signal came from the 10 mm diameter inclusion at all depths. For this reason, a phantom has been designed with 10 mm diameter inclusions containing either ICG, Er-doped ReANCs, or no contrast agent placed at depths of 1 mm, 3 mm, and 5 mm into a gelatin phantom.

3.5.2: Methods

Gelatin layers and agarose inclusions were fabricated according to the protocol outlined in Section 3.2.2. Three 10 mm diameter agarose inclusions containing either no contrast agent, 14 μ M ICG, or 0.6 mg/mL Er-doped ReANCs were synthesized using custom 3D-printed molds. A gelatin phantom was fabricated and poured layer-by-layer into a pre-chilled container to place one inclusion of each type at 1 mm, 3 mm, and 5 mm depths according to the outline in Figure 29. A final 11 mm thick layer was poured last to cover completely the inclusions embedded 5 mm deep.

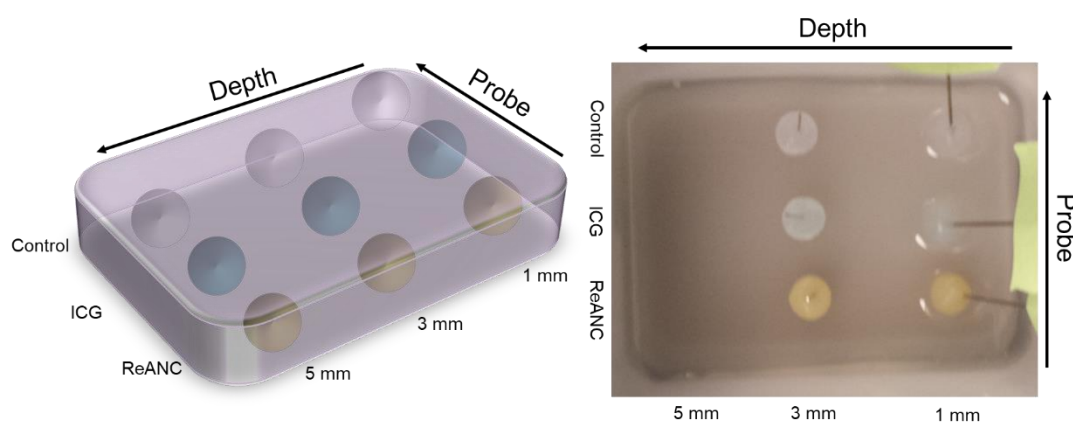


Figure 29: Phantom fabrication process for evaluation of scattering and resolution. Spherical inclusions of 10 mm diameter were placed at depths 1 mm, 3 mm, and 5 mm into a tissue-mimicking gelation phantom. Inclusions contained either no contrast agent (agarose only controls), 14 μ M ICG, or 0.6 mg/mL Er-doped ReANCs.

SWIR images were obtained using the SWIR setup from Section 2.1.4 and its accompanying software (Section 2.2). The phantom was illuminated by manually scanning a 980 nm collimated beam with 1.8 W power and area 0.785 cm² across the field of view. Images were acquired with an exposure time of 32.98 ms.

NIR images were obtained using the NIR setup from Section 2.1.4 and its accompanying software (Section 2.2). A 785 nm collimated beam with 12 mW power (380 mA current) and area 0.785 cm² was manually scanned across the field of view. Images were acquired with an exposure time of 1 ms.

All SWIR and NIR images obtained were evaluated for their scattering and resolution by examining the pixel value profile of a line drawn through each signal in ImageJ. From each inclusion's profile, the peak width for the signal was determined, where a narrower peak indicates less scattering and a broader peak suggests higher scattering. The full width of the peak at half the maximum pixel value was taken to be the peak width. Moreover, the peaks were assessed for their height, where a lower peak indicates lower signal intensity and a higher peak indicates higher signal intensity. In this way, signal intensity and scattering were determined for each contrast agent at each depth.

Post-imaging, each inclusion was resected using the overlay image as a guide. The resection was not blinded, and the person doing the resection was aware of the phantom fabrication process. The resected inclusions as well as their resection cavities

were imaged under the same conditions as the unresected phantoms and evaluated in terms of the number of inclusions out of the whole that were resected and the margin size in and outside the cavity.

3.5.3: Imaging Results

For imaging of the ReANC-containing inclusions, the 1 mm deep inclusion was apparent without scaling of the display images, but the 3 mm deep inclusion was only discernible when the overlay and SWIR images were scaled between pixel values 50 and 200 (Figure 30).

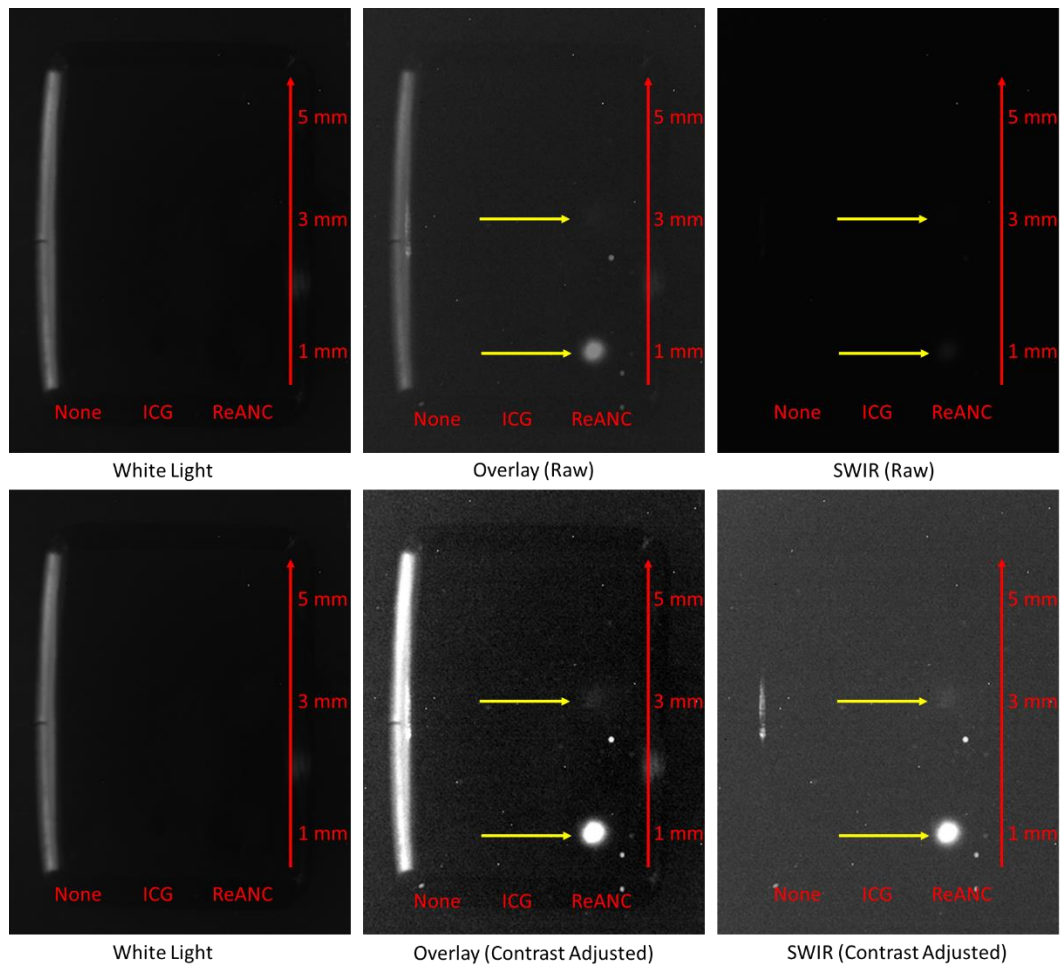


Figure 30: White light, overlay, and SWIR images of the ICG-ReANC composite phantom illuminated using the SWIR hardware and software described in Section 2.1.4 and Section 2.2. Under 980 nm / 1.8 W illumination, only the 1 mm and 3 mm deep inclusions were discernible. The ICG-containing inclusions did not emit a detectable signal in Er's emission range. Yellow arrows indicate inclusion positions. The red arrow indicates the direction of increasing inclusion depth. The raw SWIR image had a range of potential pixel values between 0 and 4095, and the contrast adjusted SWIR image was scaled between values 50 and 200 for display only.

The 5 mm deep ReANC-containing inclusion was undetectable as with the size-depth phantom (Section 3.4). Conversely, the ICG-containing inclusions were detectable at every depth despite the much lower illumination intensity and exposure time.

Interestingly, the ReANC-containing inclusions also had NIR emissions detectable at every depth and greater intensity in mean pixel value than their SWIR peaks (Figure 31). (During this NIR imaging, the phantom was flipped upside-down to minimize background noise, reversing the inclusion depths from those outlined in Figure 30).

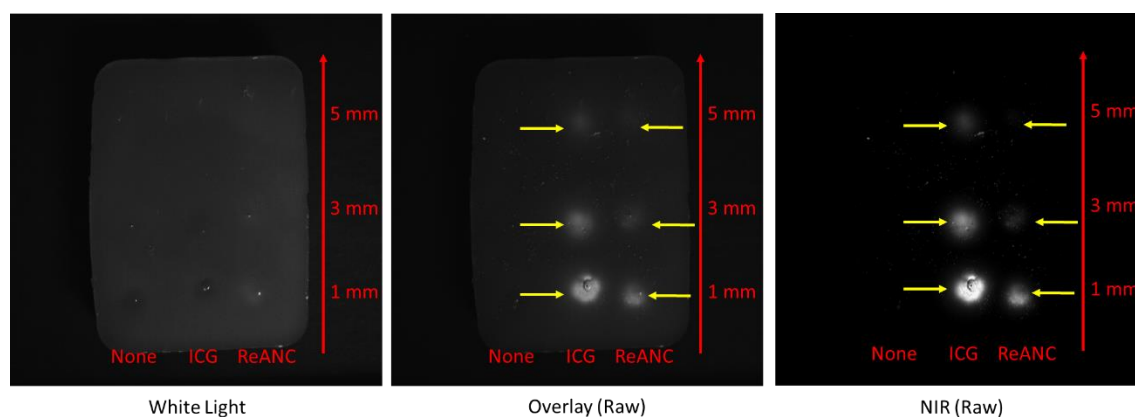


Figure 31: White light, overlay, and NIR images of the ICG-ReANC composite phantom illuminated using the NIR hardware and software described in Section 2.1.4 and Section 2.2. Under 793 nm 12 mW (380 mA) illumination, inclusions at every depth were detected for both contrast agents, suggesting that the ReANC-containing inclusions emit a detectable signal in ICG's emission range. Yellow arrows indicate inclusion positions. The red arrow indicates the direction of increasing inclusion depth.

The phantom was imaged six times with each excitation source, and the average mean pixel values and SBRs were calculated from an ROI centered around each fluorescent signal. The ICG-containing inclusions had the highest mean pixel value and SBR for every depth tested. The NIR peaks for the ReANC-containing inclusions were lower than that of the ICG-containing inclusions but higher than the SWIR peaks at every depth. By 3 mm depth, the ReANC SWIR emissions were nearly at the background level.

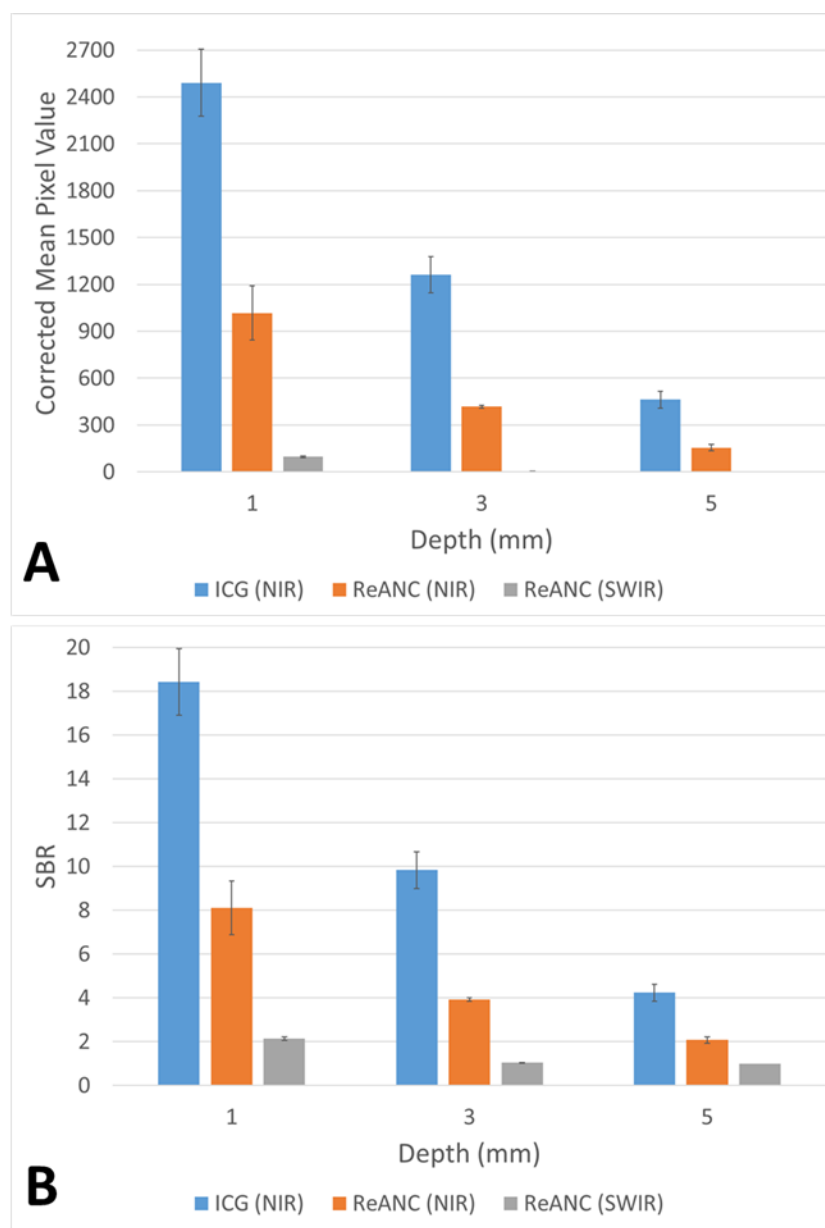


Figure 32: (A) Corrected mean pixel values for the NIR and SWIR emissions from ICG-containing and ReANC-containing inclusions at concentrations 14 μM and 0.6 mg/mL respectively at 1 mm, 3 mm, and 5 mm depths under 980 nm and 793 nm illumination. (B) The corresponding SBR values. The NIR emissions from both inclusions had higher mean pixel values and SBRs than the SWIR emissions from the ReANC-containing inclusions. Results indicate that ICG NIR emissions are the most distinguishable from background. Error bars indicate one standard deviation from the mean of the six images in each set.

To evaluate the scattering and resolution of each contrast agent, a line profile was drawn through each set of inclusions in the fluorescent images, where each peak in the profile represented an inclusion. The peak heights indicate the maximum signal intensity for the inclusion, and the full width at half maximum (FWHM) peak heights captured the extent of scattering.

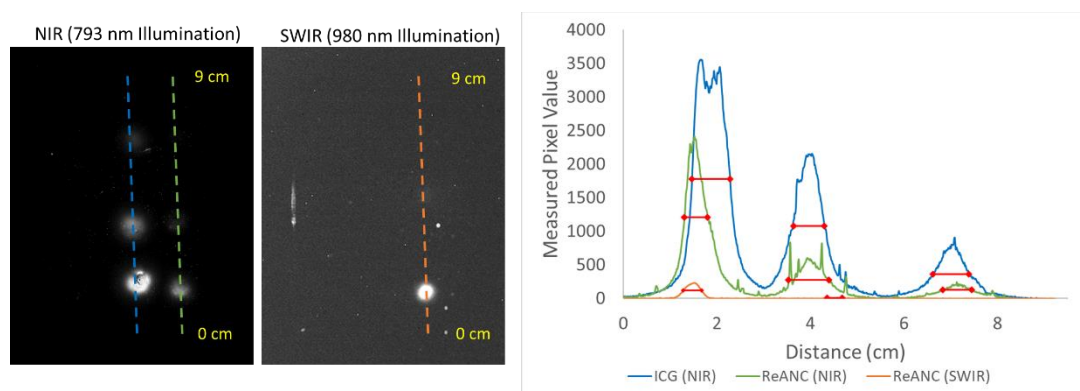


Figure 33: Line intensity profiles of the NIR and SWIR emissions from ICG-containing (14 μM) and ReANC-containing (0.6 mg/mL) inclusions at 1 mm, 3 mm, and 5 mm depths under 980 nm and 793 nm illumination. Red bars indicate the full width at half maximum peak height. The raw SWIR image had a range of pixel values between 0 and 4095, and the shown SWIR image was scaled between values 50 and 200 for display only.

Table 5: Full Width at Half Maximum (FWHM) for ICG and ReANC Inclusions				
Probe	Depth (mm)	Peak Height	1/2 Peak Height	FWHM (cm)
ICG	1	3553	1777	0.8
ICG	3	2149	1074	0.6

ICG	5	723	362	0.8
ReANC (NIR)	1	2414	1207	0.5
ReANC (NIR)	3	549	275	0.9
ReANC (NIR)	5	244	122	0.6
ReANC (SWIR)	1	231	116	0.4
ReANC (SWIR)	3	12	6	0.3

Table 5: Peak heights and widths for ICG-containing and ReANC-containing inclusions at depths 1 mm, 3 mm, and 5 mm under 980 nm and 793 nm illumination

Referring to Table 5, there was no clear trend in peak width with depth. The NIR emissions from the ICG-containing inclusions had the widest peaks while the SWIR emissions from the ReANC-containing inclusions had the narrowest peaks. However, this may be due to the much smaller peak height of the ReANC emissions compared to that of ICG, and more data are necessary to evaluate the scattering and resolution further.

3.5.4: Resection Results

ICG-containing inclusions were able to be resected at every depth while only ReANC-containing inclusions at 1 mm and 3 mm depths were able to be resected using fluorescence guidance.

Table 6: Resection Results			
Probe	Spectrum	Depth (mm)	Resected?
ICG	NIR	1	Y
ICG	NIR	3	Y
ICG	NIR	5	Y
ReANC	SWIR	1	Y
ReANC	SWIR	3	Y
ReANC	SWIR	5	N
None	Visible	1	Y
None	Visible	3	Y
None	Visible	5	Y

Table 6: Inclusions containing ICG were able to be resected at every depth using NIR guidance. The two shallowing ReANC-containing inclusions were able to be resected under SWIR guidance while the 5 mm depth inclusion was indistinguishable from the background and could not be resected. Control inclusions containing no contrast agent were resected under visual inspection and with guidance by palpation at every depth.

The remaining ReANC-containing inclusion was 5 mm from the top of the phantom and 1 mm from the bottom. By flipping the phantom over, this remaining inclusion could be imaged and resected from a 1 mm depth (Figure 34).

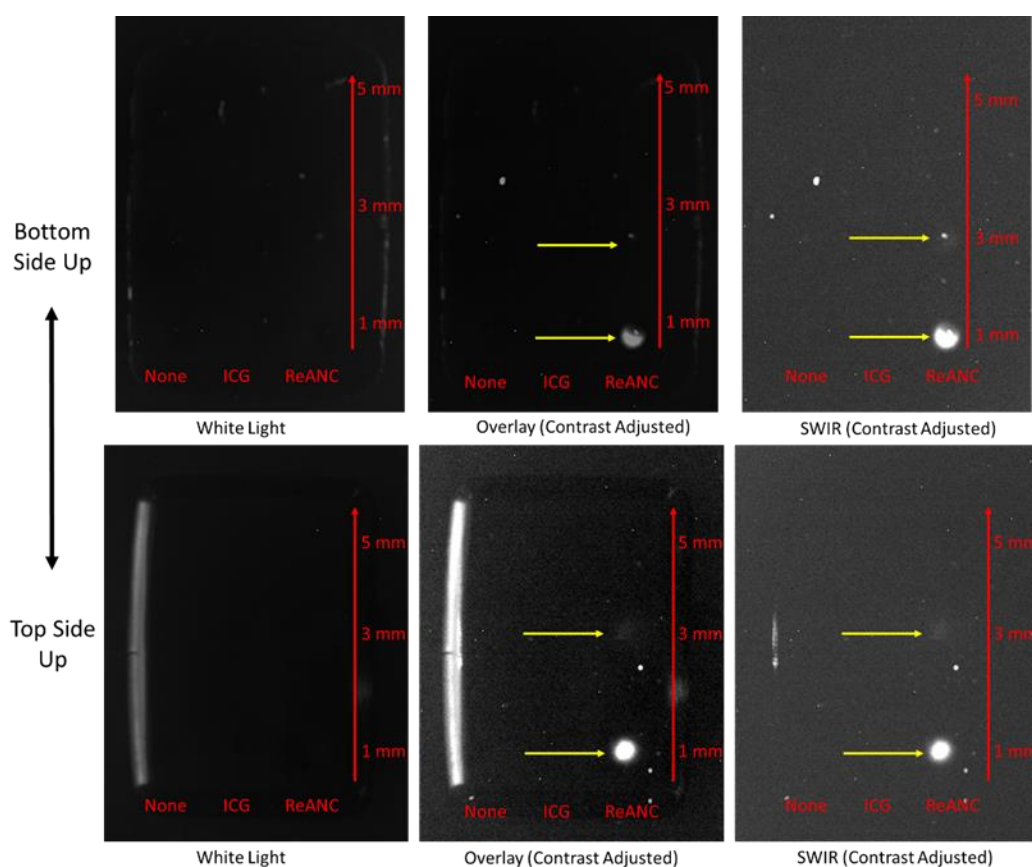


Figure 34: Flipping the ICG-ReANC composite phantom over reverses the inclusion depths, allowing the ReANC-containing inclusion previously at 5 mm deep to be imaged as a 1 mm deep inclusion. The raw SWIR images had a range of pixel values between 0 and 4095, and the contrast adjusted SWIR images were scaled between values 50 and 200 for display only.

Following resection under SWIR guidance, the ReANC-containing inclusions were resected with only a small margin of surrounding phantom. One inclusion resected at the 1 mm depth had a positive margin of about half the total inclusion remaining in the cavity (Figure 35).

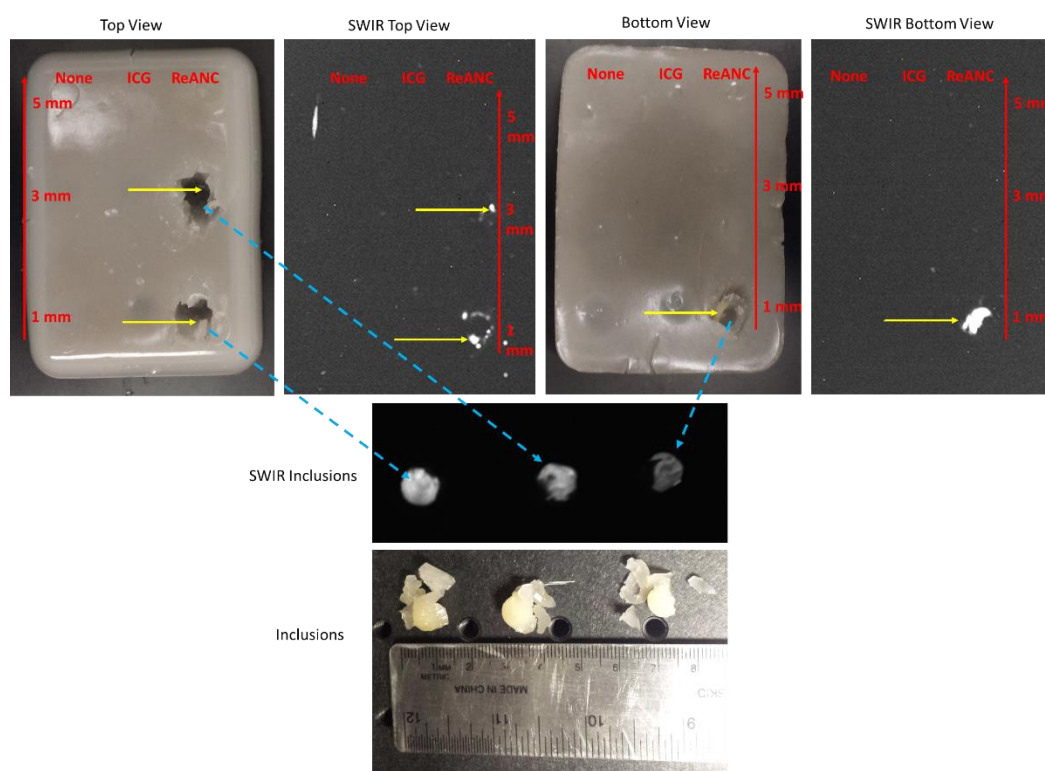


Figure 35: Resected phantoms and ReANC-containing inclusions under SWIR guidance with fluorescence images. Yellow arrows point to the positive margins in the cavities. The red arrow and text indicate the depth at which the inclusion was placed. Blue dashed arrows indicate the cavity from which the indicated inclusion was resected. The raw SWIR images had a range of pixel values between 0 and 4095, and the contrast adjusted SWIR images were scaled between values 50 and 200 for display only.

The ICG-containing inclusions were resected with slightly larger negative margins than the ReANC-containing inclusions, and every cavity had some positive margin remaining.

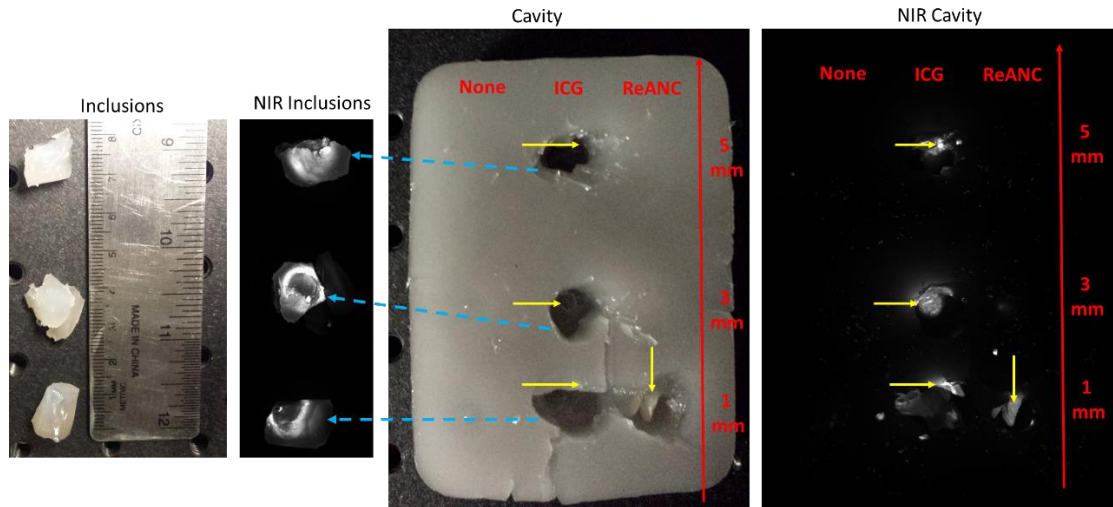


Figure 36: Resected phantoms and ICG-containing inclusions under NIR guidance with fluorescence images. Yellow arrows point to the positive margins in the cavities. The red arrow and text indicate the depths at which the inclusions were placed. Blue dashed arrows indicate the cavity from which the indicated inclusion was resected. NIR pixel values were in the range of 0 to 4095.

Comparing the SBR of the cavity and inclusions between the ReANC and ICG results, the ICG cavities had higher SBR than the ReANC cavities, with the exception of one ReANC cavity that had high positive margins.

Table 7: Inclusion and Cavity Corrected Pixel Values and SBR					
Probe	Depth (mm)	Inclusion Mean	Cavity Mean	Inclusion SBR	Cavity SBR
ICG	1	1614	1386	12.3	10.7
ICG	3	2086	1248	15.6	9.7
ICG	5	1224	703	9.6	5.9
ReANC	1	2348	22	29.5	1.3
ReANC	1	1025	974	13.2	12.6
ReANC	3	1659	53	20.7	1.6

Table 7: Mean pixel values and SBRs for resected inclusions and cavities remaining after resection with NIR guidance (ICG inclusions) and SWIR guidance (ReANC inclusions). The SBR tended to be higher for the ICG-containing inclusions.

The control inclusions containing no contrast agent were resected under guidance by visual inspection and palpation. While they left behind no positive margins, they had the largest negative margins (“healthy tissue” removed) of all the resected inclusions.

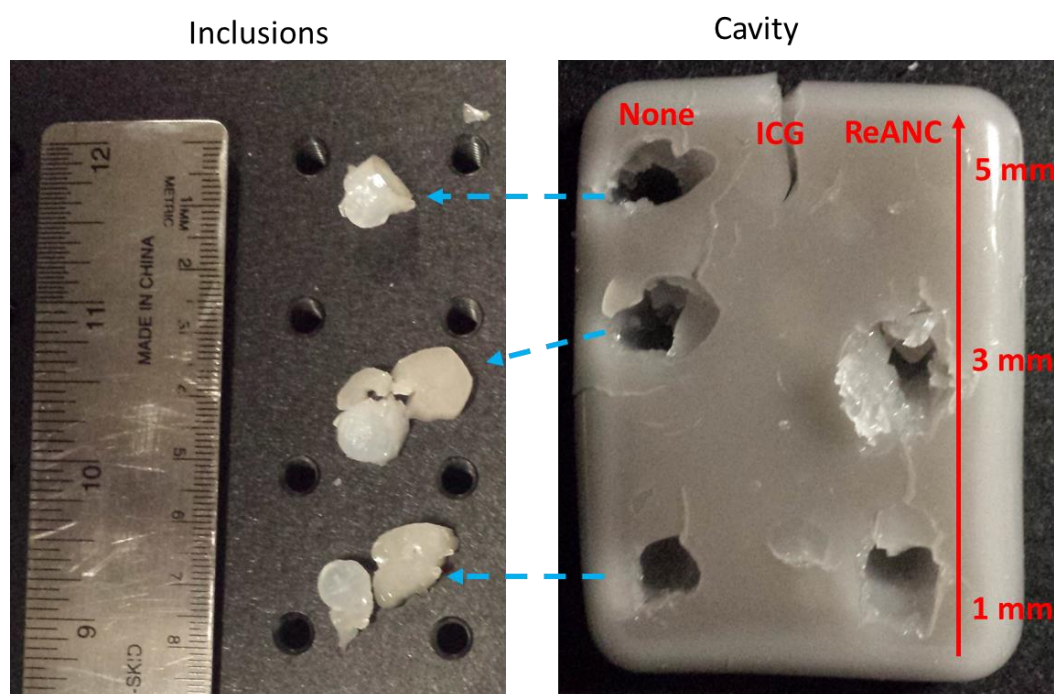


Figure 37: Resected phantoms and probe-free inclusions under visible light and palpation guidance. The red arrow and text indicate the depth at which the inclusion was placed. Blue dashed arrows indicate the cavity from which the indicated inclusion was resected.

3.6: Inclusion Shape Experiments

Tumors exist in a variety of shapes and are typically not spherical in geometry. Previous sections have evaluated the proposed SWIR imaging system using sets of uniform, spherical inclusions, but to be more biologically relevant, the accuracy of detection and resection must be evaluated with irregularly-shaped inclusions. To this end,

a phantom containing both spherical and irregularly-shaped fluorescent inclusions has been imaged and resected.

3.6.1: Phantom Design

Size-depth studies (Section 3.4) have revealed that an inclusion with a diameter of 5 mm, 7.5 mm, or 10 mm placed at a depth of either 1 mm or 3 mm could be distinguished from the background. Thus, to evaluate the effect of shape on image quality and resection accuracy, spherical and irregularly-shaped inclusions of 7.5 mm diameter and containing the contrast agent of interest were placed at 1 mm and 3 mm in a gelatin phantom.

3.6.2: Methods

To create ReANC-containing inclusions, agarose mixtures were prepared according to the fabrication protocol outlined in Section 3.2.2 and poured into molds to produce either spherical or irregular inclusions.



Figure 38: Custom molds (left) were 3D-printed and filled with agarose mixtures to produce inclusions of irregular shape (right).

91 nm diameter ReANCs were used during fabrication. Inclusions were embedded at 1 mm and 3 mm depths into a gelatin phantom according to the design in Figure 39.

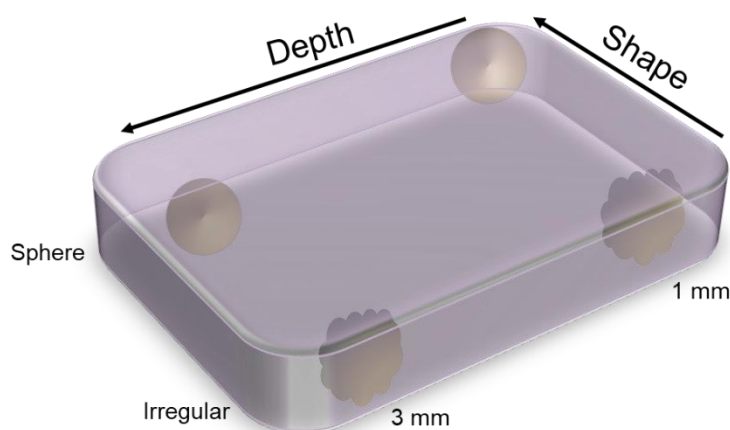


Figure 39: Phantom design for comparisons between irregularly-shaped and spherical ReANC-containing inclusions of 7.5 mm diameter placed 1 mm and 3 mm deep into a tissue-mimicking gelatin phantom.

White light images of the resulting phantom were obtained under a infrared heat lamp using the imaging setup described in Sections 2.1.4 and 2.2. SWIR and overlay images were created by manual scanning of the phantom with a 980 nm collimated beam (1.8 W power, 0.785 cm² area).

3.6.3: Imaging Results

The resolution of the system was not sufficient enough to make out the protrusions from the irregularly-shaped inclusions in great detail, though the shape of the inclusion from its SWIR emissions was discernibly irregular compared to the spherical inclusion.

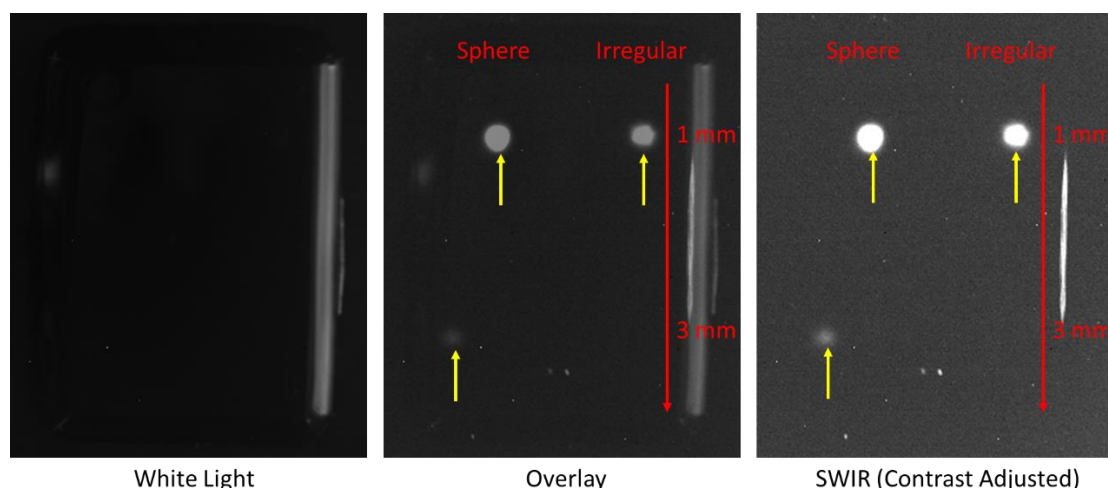


Figure 40: White light, overlay, and SWIR images of 7.5 mm diameter ReANC-containing spherical and irregularly-shaped inclusions at 0.6 mg/mL concentration and depths of 1 mm and 3 mm. The irregularly shaped inclusion is visibly non-spherical at 1 mm deep but not detectable at 3 mm deep. The raw SWIR image had a range of pixel values between 0 and 4095, and the contrast adjusted SWIR image was scaled between values 50 and 200 for display only.

The 3 mm deep irregularly-shaped inclusion was not detectable at 3 mm deep. The spherical inclusion, while detectable at 3 mm deep, had an SBR of nearly 1. The measured mean pixel values and SBR were higher for the spherical inclusions at both depths. Six images were scanned and averaged for the final values.

Table 8: Mean Corrected Pixel Values and SBRs for Spherical vs. Irregularly-Shaped Inclusions					
Shape	Depth (mm)	Background Corrected Mean	Std Dev Corrected Mean	SBR	Std Dev SBR
Sphere	1	710	47	9.3	0.6
Sphere	3	15	3	1.2	0.0
Irregular	1	209	29	3.4	0.3

Table 8: Background-corrected mean pixel values and SBRs for irregularly-shaped and spherical inclusions containing 0.6 mg/mL ReANCs and placed 1 mm and 3 mm deep into a tissue-simulating gelatin phantom. Standard deviations represent the variation in six consecutive images of the phantom.

3.6.4: Resection Results

The cavity left behind after resecting the spherical inclusions had a lower SBR than the irregularly-shaped inclusion cavity, indicating better resection of a spherical inclusion over the irregular inclusion. Despite this, the sample size is too low to draw definitive conclusions, and more data are necessary to analyze the effect of inclusion shape on resection accuracy. However, the preliminary findings here suggest that the simpler the inclusion shape, the greater the accuracy of resection.

Table 9: Resection Results for Spherical and Irregularly-Shaped Inclusions					
Shape	Depth (mm)	Cavity Mean Pixel Value	Resected Inclusion Mean Pixel Value	Cavity SBR	Inclusion SBR
Sphere	1	14	1605	0.2	18.8
Sphere	3	0	1804	0.0	21.1
Irregular	1	248	2163	2.9	25.3

Table 9: Background-corrected mean pixel values and SBRs for resected irregularly-shaped and spherical inclusions and their cavities.

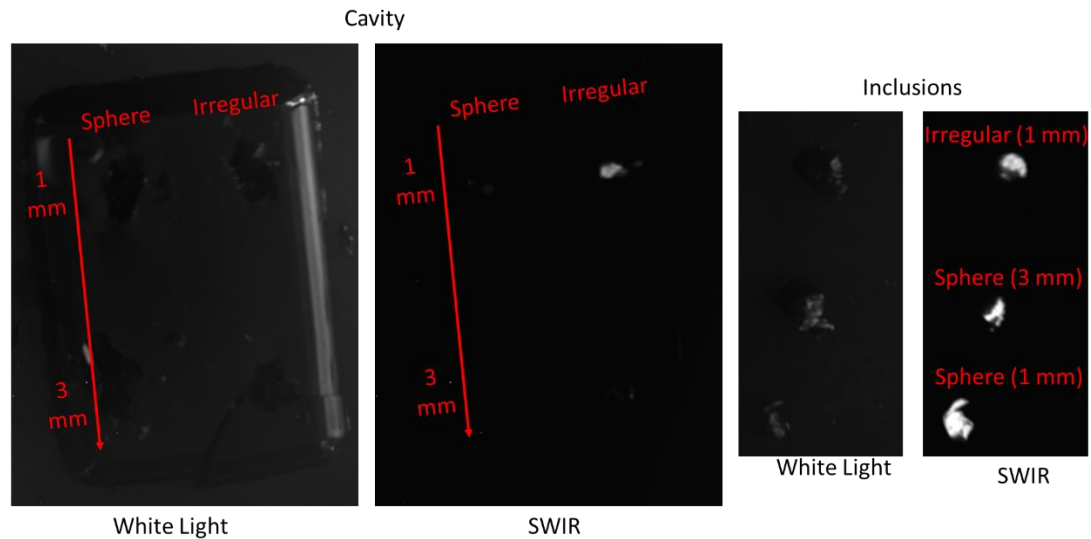


Figure 41: White light and SWIR images of the imaged cavity and inclusions show highest positive margins for the irregularly-shaped inclusion at 1 mm depth. SWIR pixel values ranged between 0 and 4095.

3.7: Discussion

3.7.1: Discussion of Imaging Results

From the experiments with both chicken breast and gelatin phantoms (Section 3.3 and Section 3.4), signal mean pixel value and SBR decreased with increasing depth and decreasing inclusion diameter (Figures 19, 21, 22, 26, 25). This suggests that for lesions tagged with ReANCs, larger-sized lesions will be more readily-detected at each depth and that size and depth limit the detection capabilities of the proposed SWIR imager. While further investigation is required to determine the smallest resolvable lesion size, it appears that 5 mm is the limiting depth of resolution for ReANC-targeted lesions at biologically relevant concentrations.

The sample size for the experiments performed in Section 3.5 is too low to draw definitive conclusions about the imaging quality of ICG versus the Er-doped ReANCs; however, the preliminary results of these experiments lead to the following conclusions. 10 mm diameter ICG-containing inclusions imaged in Section 3.5 had signals with $SBR > 1$ at 1 mm, 3 mm, and 5 mm depths. These signals were higher in mean pixel value and SBR at every depth than signals from the same sized inclusions containing ReANCs. Furthermore, ICG-containing inclusions had strong signals under low power illumination (12 mW) and low exposure time image acquisition (1 ms) whereas the weaker signals obtained from the ReANCs required much higher power (1.8 W) and longer exposure time (32.98 ms). The quantum efficiency for the Zyla 5.5 sCMOS camera (Andor) is approximately 25% at ICG's emission peak (840 nm) while the quantum efficiency for the SUI640HSX-1.7RT (Sensors Unlimited) is approximately 80% at the Er-doped ReANC's emission peak (1525 nm). Therefore, the differences in

mean pixel value and SBR are unlikely to be due to a higher sensitivity of the NIR camera over the SWIR camera.

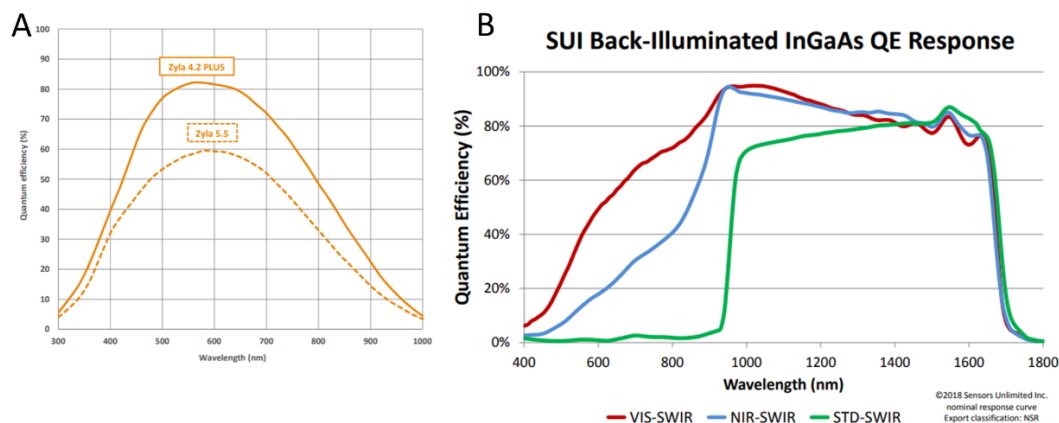


Figure 42: (A) Quantum efficiency for the NIR-sensitive Zyla 5.5 sCMOS camera (Andor) [39]. (B) Quantum efficiency for the SWIR-sensitive SUI640HSX-1.7RT camera (Sensors Unlimited) [40].

Similarly, the filters coupled to each camera were comparable in their ability to limit background noise. For a 12-bit range (0 to 4095), the background level during NIR detection averaged around 140 counts and was consistently greater than the background level during SWIR detection, which averaged around 80 counts, despite the shorter exposure time used in NIR imaging. This may be due to the NIR camera receiving more ambient light from the room lights which emit more in the vis / NIR range than in the SWIR. Overall, the SWIR and NIR imaging setups had similar sensitivities and background noise. For this reason, differences in SBR between ICG and the ReANCs are likely due to differences between the contrast agent rather than the imaging setup.

From the experiments outlined in Section 3.5, it is evident that ICG at the 14 μM concentration has a greater penetration depth through tissue than ReANCs at the biologically relevant concentration of 0.6 mg/mL, producing higher SBR signals at 5 mm

depths. This may be in part due to the differences between the two probes in quantum yield and optical efficiency, which represent the ratio of emitted to absorbed photons and the ratio of emitted to incident power respectively. ICG has been reported to have a quantum yield of 9.3% while the Er-doped ReANCs have an optical efficiency of 1.17% [37-38]. The brighter detected signal from ICG seen in Section 3.5 could therefore be attributed to a higher emission efficiency.

Another factor that may contribute to ICG's higher penetration depth is the proximity of the Er-doped ReANCs' 1525 nm emission peak to a peak in the water absorption spectrum. Meanwhile the 840 nm ICG emission peak is clear of such a peak (Figure 43).

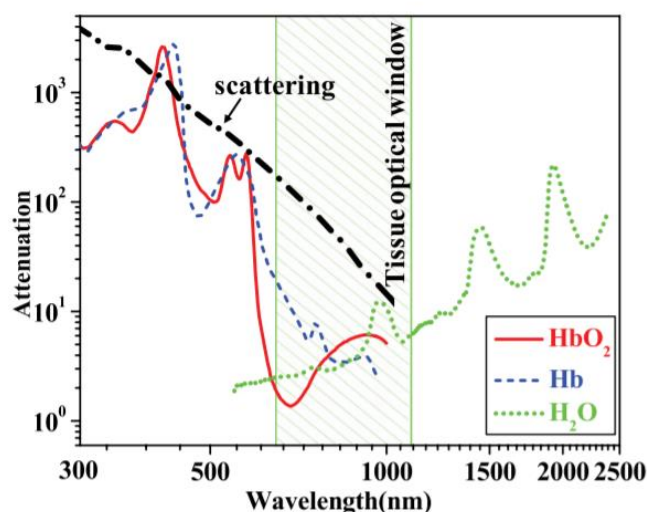


Figure 43: Absorption spectra for water (green), deoxy-hemoglobin (blue) and oxy-hemoglobin (red). Reproduced from [41] with permission from AIP Publishing.

The ReANC emissions are absorbed far more by water in the tissue-mimicking phantom than those from ICG. This reduction in absorption dominates so that Er-doped ReANC emissions are attenuated more than ICG emissions in tissue despite their lower

scattering. Likewise, the high SBR of ICG over the ReANCs suggest that lesions targeted with ICG will be more discernible from healthy tissue than those tagged with Er-doped ReANCs.

The ReANC-containing inclusions had emissions detected in both the NIR and SWIR ranges while the ICG-containing inclusions were only detectable in the NIR. The NIR emissions from the ReANC-containing inclusions had greater mean pixel values and SBRs than their SWIR emissions at every depth. This coupled with the ability to detect the 5 mm deep ReANC-containing inclusion using an NIR-sensitive camera indicate that further investigation into the origin of these NIR emissions from Er-doped ReANC inclusions may be useful for imaging with greater penetration depth.

The NIR emissions from the ICG-containing inclusions had greater peak widths than the SWIR emissions from the ReANC-containing inclusions. This may be due to the lower scattering in tissue of the longer 1525 nm emissions over the 840 nm emissions, but more data is required to evaluate the differences in scattering and resolution between the two contrast agents.

From the experiments performed in Section 3.6, it was seen that the features of the irregularly-shaped inclusion were lost when placed in a tissue-mimicking phantom. Likely, the attenuation of the SWIR emissions by the phantom as well as the limitations of the imaging setup limit the imaging resolution. While the detected fluorescent signal was visibly irregular in shape, the finer details of the inclusion were not preserved. This may limit lesion detection during FGS as lesions are typically irregular with variably-sized appendages.

3.7.2: Discussion of Resection Results

In the experiments in Section 3.5, all of the ICG-containing inclusions and control inclusions were resected at every depth while only ReANC-containing inclusions at 1 mm and 3 mm depths were resected. This can be attributed to the higher penetration depth of ICG over the Er-doped ReANCs discussed in Section 3.7.1. The signal strength of the ReANCs was so much weaker than the ICG that resection was hindered by low SBR at the 5 mm depth.

It was found that the ReANC-containing inclusions resected under SWIR guidance had the smaller negative and positive margins than the ICG-containing inclusions resected under NIR guidance. This indicates that targeting lesions with Er-doped ReANCs may improve the accuracy of surgical resection over guidance using ICG. Resection under visible light inspection and palpation produced the highest negative margins, indicating that FGS using either ICG or the Er-doped ReANCs may limit resection of healthy tissue. As the study was not blinded and the sample size low, more data are required to validate this hypothesis.

From the Section 3.6 experiments, spherical inclusions were resected with smaller positive margins than irregularly-shaped inclusions, as indicated by the significantly lower SBR of the spherical inclusion cavities compared to the irregular inclusion cavity. Because the finer features of the irregularly-shaped inclusions are lost from the fluorescent image upon attenuation by the surrounding medium, resection accuracy is diminished. Only one irregularly-shaped inclusion was able to be seen and resected, necessitating further studies to confirm these findings.

CHAPTER 4: CONCLUSIONS

4.1: Discussion of Results and Comparison to Literature

Based on the experiments performed in Chapter 3 with chicken breast and gelatin phantoms, this work has culminated in the following conclusions. Inclusions containing a biologically relevant concentration of Er-doped ReANCs (0.6 mg/mL) can be detected up to 5 mm deep into tissue. Mean pixel values and SBR for agarose ReANC-containing inclusions diminished with increasing depth and became negligible past 5 mm deep in both chicken breast and gelatin phantoms. Previously, Naczynski *et al.* found that 1525 nm light could penetrate twice as far, up to 10 mm through tissue-mimicking agarose phantoms [21]. The disparity between these results can be attributed to the differences in illumination. In the experiments reported in Section 3, both the illumination and excitation beam were required to travel through the phantom so that both beams were attenuated. However, in the experiments performed by Naczynski *et al.*, the illumination beam did not travel through a phantom, and the incident light hitting the rare earths was unattenuated [21]. Had the illumination beam had to pass through a tissue-mimicking phantom to reach the rare earths, then the incident excitation light would have been more attenuated and the measured penetration depth likely would have been lower.

Zevon *et al.* additionally found that Er-doped ReANCs enabled detection of metastatic breast cancer lesions $<30 \text{ mm}^3$ (approximately 2 mm in diameter) up to 11 mm into athymic nude mouse lungs [29]. However, light absorption at 1525 nm in the mouse lungs is low compared to most other tissues (Figure 44), suggesting that decreased absorption in the lungs may be responsible for this observation. While it was previously believed that the diminished scattering of ReANC SWIR emissions could overcome

increased water absorption, the effects of water absorption on SWIR penetration depth appear too strong to be neglected. For this reason, SWIR-emitting ReANCs do not necessarily provide increased penetration depth, a factor that can limit their usefulness in deep tissue imaging.

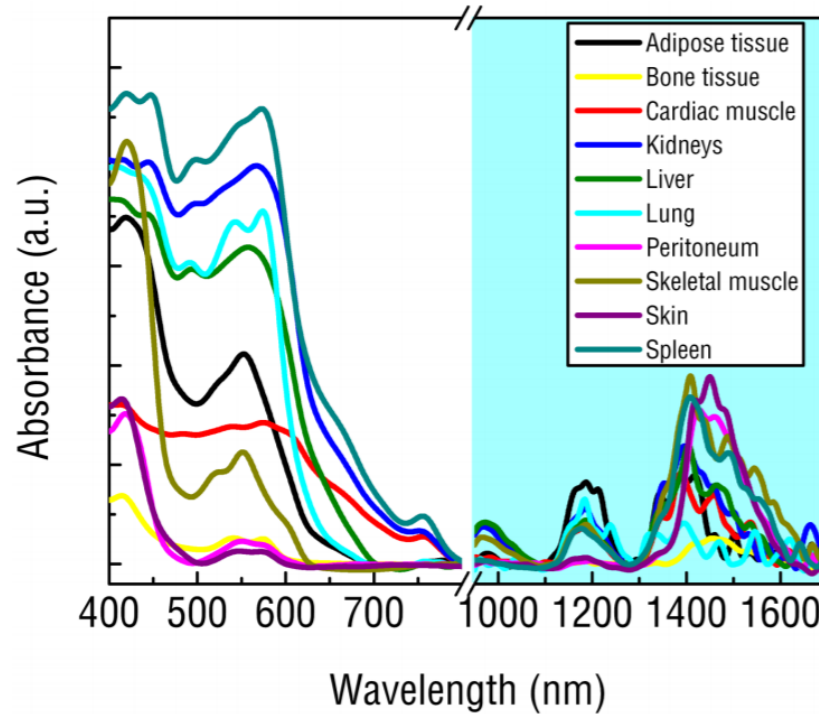


Figure 44: Absorption spectra measured for varying athymic nude mouse tissues indicate lowest absorption of 1525 nm light in the lungs and bone tissue. Reproduced from [21] with permission from Springer Nature.

The size-depth phantom studies in Section 3.4 indicated that increasing lesion depth and decreasing lesion size diminished the likelihood of SWIR detection. Mean pixel value and SBR dramatically decreased with only millimeter increases in lesion depth, indicating a sensitivity of the proposed FGS system to lesion depth. Moreover, both mean pixel value and SBR decreased with decreasing inclusion size, suggesting that, for lesions containing the same concentration of ReANCs, larger lesions will be more easily distinguished from background tissue fluorescence at every depth.

In Section 3.5 it was found that, while the Er-doped ReANCs were limited to 5 mm penetration depth at 0.6 mg/mL, ICG at a 14 μ M concentration could be detected at greater depths with higher mean pixel value and SBR. Pleijhuis *et al.* had previously found the limiting penetration depth of ICG at the same concentration and embedded in similar gelatin-mimicking phantoms to be 21 mm, far beyond that observed here with Er-doped ReANCs [20].

ICG detection required lower intensity illumination and shorter exposure times at higher lens f-number compared to ReANCs. This is advantageous in a surgical setting where lower intensity illumination presents less risk to the patient. Likewise, ICG detection produces more light per second at the camera than with ReANC detection, which requires higher intensity illumination at longer exposure times and a lower f-number lens. Even more compelling was that the NIR camera had lower quantum efficiency within ICG's emission range than the SWIR camera had at the Er-doped ReANCs' emission range, insinuating that differences in detection efficiency were due to differences between the contrast agents rather than camera sensitivity. Notably, the Er-doped ReANCs also exhibited peaks in the NIR range that were stronger at every depth than their SWIR emissions but lower in mean pixel value than ICG's NIR emissions. Under 980 nm illumination, Er is known to produce upconversion light, or emissions less than 980 nm in wavelength, commonly seen in the red and green visible light regions. However, these are not expected to transmit through the NIR system's bandpass filter, and further investigation is required to determine the exact mechanism for this emission. Overall, ICG is more easily-detected than Er-doped ReANCs under the given imaging

conditions, and lesions targeted with ICG at 14 μM concentration are more readily distinguished from background than Er-doped ReANCs at *in vivo* concentrations.

Despite the advantages of ICG in signal detection over the Er-doped ReANCs, inclusions containing ReANCs were resected with greater accuracy on the whole, as indicated by the lower SBR of the ReANC resection cavities. Still, ICG inclusions could be resected at all depths while the 5 mm deep ReANC inclusion could neither be detected nor resected. Likewise, one ReANC-containing inclusion at 1 mm depth had a large positive margin, suggesting that more data needs to be collected to properly evaluate resection accuracy with either probe.

Based on the findings from Section 3.5, ICG is a better candidate for FGS imaging than ReANCs, but there are limitations in its use that need to be addressed. ICG is an untargeted dye with a recommended 2.5 mg/mL (3226 μM) intravenous dose in adults, though the dosage is known to vary. The concentration of ICG administered tends to be higher than the 14 μM ideal concentration, but because it is untargeted, the final concentration of ICG at a tumor site is likely to be much lower and variable.

Additionally, Pleijhuis *et al.* determined that emission strength does not increase linearly with ICG concentration due to self-quenching effects [20]. Thus, in order for ICG to be a practical imaging agent in guided tumor resection, the probe delivery and composition must be modified to precisely control the final concentration at the tumor sites. In recent years, there has been some focus on creating targeted ICG conjugates. For instance, ICG has been successfully conjugated with the monoclonal antibodies daclizumab (Dac), trastuzumab (Tra), or panitumumab (Pan), enabling specific visualization of CD25-expressing, HER1+, or HER2+ tumors respectively [42]. The limitation of developing

such agents is that they would need to go through the FDA approval process. However, since ICG is already FDA-approved, ICG conjugates may be more easily translated to the clinic than targeted ReANCs.

The final experiments in this study investigated the effect of inclusion shape on image quality and resection accuracy. In Section 3.6, it was found that for 7.5 mm diameter ReANC-containing inclusions, resolution of irregularly-shaped inclusion appendages was limited, and spherical inclusions were resected more accurately and left behind less positive margins. Based on this, resection accuracy in future *in vivo* studies may be poorer than seen here due to irregularities in tumor shape.

4.2: Future Direction

Having validated the SWIR imaging system in tissue-mimicking phantoms, it is necessary to further validate the system *in vivo*, which will allow for better understanding of ReANC imaging capabilities in a live organism and easier translation to in-human use.

4.2.1: Small Animal Imaging

Two female athymic homozygous nude mice (Taconic) were anaesthetized and imaged pre- and post-injection with 200 μ L of 2 mg/mL Er-doped ReANCs using the hardware outlined in Section 2.1.4. Images were taken using both the LabVIEW-based software described in Section 2.2 and the camera's software (Sensors Unlimited). Neither mouse had tumors, and the majority of the ReANCs cleared to the liver. Figure 45 shows the white light, fluorescent (SWIR), and overlay images taken using the LabVIEW software (Section 2.2).

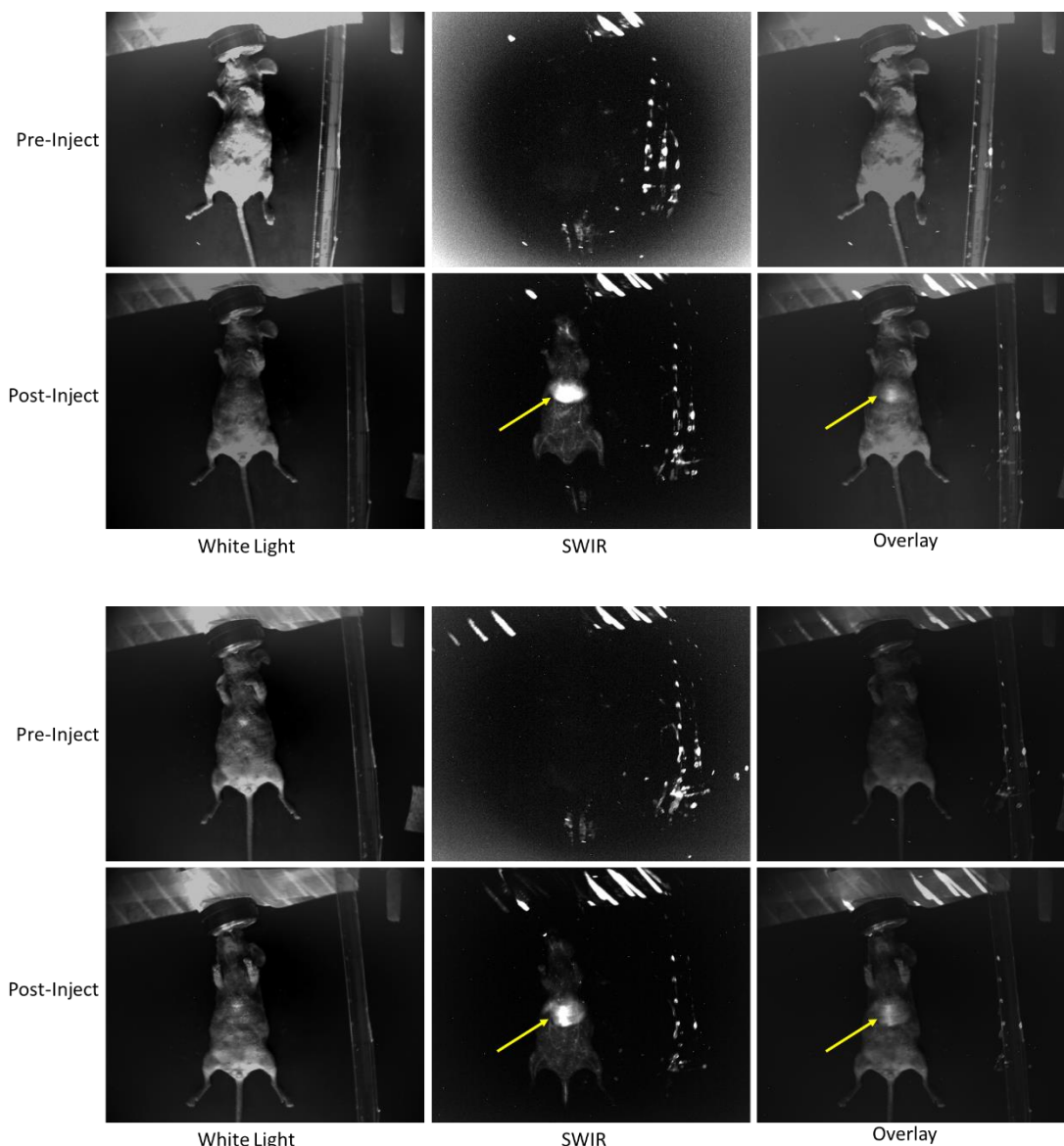


Figure 45: White light, SWIR, and overlay images of a female nude mice taken pre- and post-injection of 2 mg/mL Er-doped ReANCs using the novel SWIR imaging system (Section 2.1.4 and 2.2). The yellow arrow indicates the SWIR signal from the liver. Weaker fluorescent signal from the vasculature is apparent in both SWIR post-injection images as the time between imaging and injection was too short to allow all ReANCs to clear.

A fluorescent signal from the liver was apparent in both the SWIR and overlay images for the post-injection mice while the pre-injection images showed only

background pixel values, indicating that the SWIR signals from the mouse are from areas of high ReANC concentration.

The mice were imaged pre- and post-injection also using the SUI software, and colormapped SWIR and overlay images were created using an in-house MATLAB-based post-processing graphical user interface (GUI). In brief, white light and SWIR pre- and post-injection images were loaded into the GUI. An ROI was drawn manually on the pre-injection image using anatomical landmarks and adjusted on the post-injection image to account for changes in the mouse's position. The mean pixel value of the pre-injection SWIR image ROI (background) and the mean pixel value of the post-injection SWIR image ROI (signal) were both calculated. A background-corrected SWIR image was calculated by subtracting the mean pre-injection SWIR pixel value from the post-injection SWIR image. This corrected image was colormapped to pixel values between 20 and 200 and overlaid on top of the post-injection white light image (Figure 46).

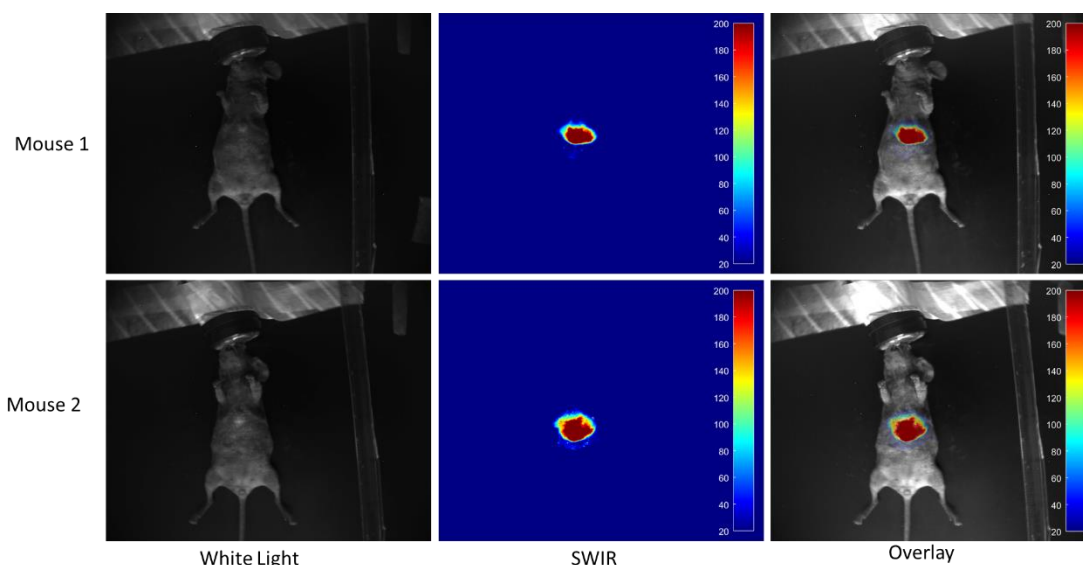


Figure 46: White light, SWIR, and overlay images of a female nude mice taken post-injection of 2 mg/mL Er-doped ReANCs using the Sensors Unlimited Inc. (SUI) software. Values were colormapped between 20 and 200.

Table 10: Mean Pixel Values for Small Animal Imaging						
	Mouse 1			Mouse 2		
Platform	PreInject	PostInject	Corrected PostInject	PreInject	PostInject	Corrected PostInject
LabVIEW	82	161	80	81	200	118
SUI	83	168	85	82	204	122

Table 10: Mean pixel values for the liver of two female nude mice pre- and post-injection with 2 mg/mL Er-doped ReANCs. Values were found using both the novel LabVIEW-based software (Section 2.2) and the Sensors Unlimited Inc. (SUI) software provided with the camera. Corrected post-injection mean pixel values were calculated by subtracting the mean pre-injection pixel value from the mean post-injection pixel value. Values were in agreement for both platforms.

The mean pixel values between the LabVIEW images and SUI images closely match, with a coefficient of variation less than 5% for all images, and the measured values lie within a similar range to a 5 mm ReANC inclusion (0.6 mg/mL) placed 1 mm to 2 mm below chicken breast (Figure 21, Section 3.3). They are likewise within the range of 5 mm diameter inclusions placed 1 mm deep in the tissue-mimicking gelatin phantoms described in Section 3. This suggests that the phantom study was biologically relevant; however, the sample size ($n = 2$) is too small for this to be considered statistically significant. More data are necessary to evaluate the biological relevance of the novel platform and the accuracy of *in vivo* resection.

4.3: Summary and Conclusions

This work focused on assessing the efficacy of Er-doped ReANCs as imaging agents to improve accuracy of tumor excision during surgery. Given the results, clinically-available ICG appears to be a more suitable imaging agent for fluorescence-guided resection of cancerous lesions. To detect tumors deeper than 5 mm beneath the tissue surface, tumors should be labeled with ICG at a 14 μM concentration, which offers

a higher SBR than Er-doped ReANCs at 0.6 mg/mL. For shallow tumors up to 3 mm into the body, Er-doped ReANCs may facilitate more accurate resection by imaging with higher resolution. Water absorption will limit Er-doped ReaNC detection, so tissues with lower water content may be more amenable to FGS with Er-doped ReANCs.

Scattering and resolution experiments (Section 3.5) and shape experiments (Section 3.6) are limited in their low sample size. Only one phantom was imaged and resected per experiment. Though human error was limited by capturing multiple images per phantom, a higher number of phantoms must be fabricated, imaged, and resected to obtain statistically significant results. Resection was further limited by lack of blinding of the study. The person performing the resection was aware of the phantom fabrication process and phantom design. To limit bias and assess inter-person variability in future work, resections must be blinded and performed by multiple parties.

The phantom study presents opportunities for an abundance of future studies. Here, the efficacy of Er-doped ReANCs and ICG have been examined in the context of tissue-simulating phantoms that offer precise control over inclusions size, shape, depth, and probe concentration. In further assessment of Er-doped ReANCs and other imaging agents the methods outlined in this phantom study may be employed to achieve high reproducibility. While phantom studies are useful for assessing imaging and resection under controlled conditions, *in vivo* studies provide data more translatable to the clinic. As shown in Section 4.2, pilot *in vivo* studies have begun to evaluate detection of Er-doped ReANCs using the novel SWIR imaging platform presented here. It is recommended that future work focus on ICG and ReANC detection in *in vivo* mouse models to draw comparisons in a context closer to in-human conditions.

REFERENCES

- [1] *Cancer Facts & Figures 2018*. Atlanta, GA: American Cancer Society, 2018, pp. 1-71.
- [2] R. Siegel, K. Miller and A. Jemal, "Cancer statistics, 2017", *CA: A Cancer Journal for Clinicians*, vol. 67, no. 1, pp. 7-30, 2017. Available: 10.3322/caac.21387 [Accessed 4 April 2019].
- [3] K. Miller et al., "Cancer treatment and survivorship statistics, 2016", *CA: A Cancer Journal for Clinicians*, vol. 66, no. 4, pp. 271-289, 2016. Available: 10.3322/caac.21349 [Accessed 4 April 2019].
- [4] K. Tipirneni et al., "Oncologic Procedures Amenable to Fluorescence-guided Surgery", *Annals of Surgery*, vol. 266, no. 1, pp. 36-47, 2017. Available: 10.1097/sla.0000000000002127 [Accessed 4 April 2019].
- [5] G. Schwartz et al., "Consensus Conference on Breast Conservation", *Journal of the American College of Surgeons*, vol. 203, no. 2, pp. 198-207, 2006. Available: 10.1016/j.jamcollsurg.2006.04.009 [Accessed 4 April 2019].
- [6] Q. Tummers et al., "Real-time intraoperative detection of breast cancer using near-infrared fluorescence imaging and Methylene Blue", *European Journal of Surgical Oncology (EJSO)*, vol. 40, no. 7, pp. 850-858, 2014. Available: 10.1016/j.ejso.2014.02.225 [Accessed 4 April 2019].
- [7] A. DSouza, H. Lin, E. Henderson, K. Samkoe and B. Pogue, "Review of fluorescence guided surgery systems: identification of key performance capabilities beyond indocyanine green imaging", *Journal of Biomedical Optics*, vol. 21, no. 8, p. 080901, 2016. Available: 10.1117/1.jbo.21.8.080901 [Accessed 4 April 2019].
- [8] J. Frangioni, "In vivo near-infrared fluorescence imaging", *Current Opinion in Chemical Biology*, vol. 7, no. 5, pp. 626-634, 2003. Available: 10.1016/j.cbpa.2003.08.007 [Accessed 4 April 2019].
- [9] E. Altinoğlu and J. Adair, "Near infrared imaging with nanoparticles", *Wiley Interdisciplinary Reviews: Nanomedicine and Nanobiotechnology*, vol. 2, no. 5, pp. 461-477, 2010. Available: 10.1002/wnan.77 [Accessed 4 April 2019].
- [10] G. Menéndez, F. Leskow and C. Spagnuolo, "Basic Concepts of Fluorescence and Fluorescent Probes", *Fluorescence Imaging for Surgeons*, pp. 3-18, 2015. Available: 10.1007/978-3-319-15678-1_1 [Accessed 4 April 2019].
- [11] G. van Dam et al., "Intraoperative tumor-specific fluorescence imaging in ovarian cancer by folate receptor- α targeting: first in-human results", *Nature Medicine*, vol. 17, no. 10, pp. 1315-1319, 2011. Available: 10.1038/nm.2472 [Accessed 4 April 2019].
- [12] J. Predina et al., "Identification of a Folate Receptor-Targeted Near-Infrared Molecular Contrast Agent to Localize Pulmonary Adenocarcinomas", *Molecular Therapy*, vol. 26, no. 2, pp. 390-403, 2018. Available: 10.1016/j.ymthe.2017.10.016 [Accessed 4 April 2019].
- [13] C. Heath, N. Deep, L. Sweeny, K. Zinn and E. Rosenthal, "Use of Panitumumab-IRDye800 to Image Microscopic Head and Neck Cancer in an Orthotopic Surgical Model", *Annals of Surgical Oncology*, vol. 19, no. 12, pp. 3879-3887, 2012. Available: 10.1245/s10434-012-2435-y [Accessed 4 April 2019].

- [14] K. Adams et al., "Comparison of visible and near-infrared wavelength-excitabile fluorescent dyes for molecular imaging of cancer", *Journal of Biomedical Optics*, vol. 12, no. 2, p. 024017, 2007. Available: 10.1117/1.2717137 [Accessed 4 April 2019].
- [15] P. Wang et al., "NIR-II nanoprobes in-vivo assembly to improve image-guided surgery for metastatic ovarian cancer", *Nature Communications*, vol. 9, no. 1, 2018. Available: 10.1038/s41467-018-05113-8 [Accessed 4 April 2019].
- [16] L. Sordillo, Y. Pu, S. Pratavieira, Y. Budansky and R. Alfano, "Deep optical imaging of tissue using the second and third near-infrared spectral windows", *Journal of Biomedical Optics*, vol. 19, no. 5, p. 056004, 2014. Available: 10.1117/1.jbo.19.5.056004 [Accessed 4 April 2019].
- [17] S. Gioux, H. Choi and J. Frangioni, "Image-Guided Surgery Using Invisible Near-Infrared Light: Fundamentals of Clinical Translation", *Molecular Imaging*, vol. 9, no. 5, pp. 7290.2010.00034, 2010. Available: 10.2310/7290.2010.00034 [Accessed 4 April 2019].
- [18] B. Zhu and E. Sevcik-Muraca, "A review of performance of near-infrared fluorescence imaging devices used in clinical studies", *The British Journal of Radiology*, vol. 88, no. 1045, p. 20140547, 2015. Available: 10.1259/bjr.20140547 [Accessed 4 April 2019].
- [19] M. Miwa, "Photodynamic Characteristics of ICG Fluorescence Imaging", *ICG Fluorescence Imaging and Navigation Surgery*, pp. 3-7, 2016. Available: 10.1007/978-4-431-55528-5_1 [Accessed 4 April 2019].
- [20] R. Pleijhuis et al., "Near-infrared fluorescence (NIRF) imaging in breast-conserving surgery: Assessing intraoperative techniques in tissue-simulating breast phantoms", *European Journal of Surgical Oncology (EJSO)*, vol. 37, no. 1, pp. 32-39, 2011. Available: 10.1016/j.ejso.2010.10.006 [Accessed 4 April 2019].
- [21] D. Naczynski et al., "Rare-earth-doped biological composites as in vivo shortwave infrared reporters", *Nature Communications*, vol. 4, no. 1, 2013. Available: 10.1038/ncomms3199 [Accessed 4 April 2019].
- [22] G. Hong et al., "Through-skull fluorescence imaging of the brain in a new near-infrared window", *Nature Photonics*, vol. 8, no. 9, pp. 723-730, 2014. Available: 10.1038/nphoton.2014.166 [Accessed 4 April 2019].
- [23] Z. Starosolski, R. Bhavane, K. Ghaghada, S. Vasudevan, A. Kaay and A. Annapragada, "Indocyanine green fluorescence in second near-infrared (NIR-II) window", *PLOS ONE*, vol. 12, no. 11, p. e0187563, 2017. Available: 10.1371/journal.pone.0187563 [Accessed 4 April 2019].
- [24] U. Resch-Genger, M. Grabolle, S. Cavaliere-Jaricot, R. Nitschke and T. Nann, "Quantum dots versus organic dyes as fluorescent labels", *Nature Methods*, vol. 5, no. 9, pp. 763-775, 2008. Available: 10.1038/nmeth.1248 [Accessed 4 April 2019].
- [25] G. Hong, A. Antaris and H. Dai, "Near-infrared fluorophores for biomedical imaging", *Nature Biomedical Engineering*, vol. 1, no. 1, p. 0010, 2017. Available: 10.1038/s41551-016-0010 [Accessed 4 April 2019].
- [26] J. Robinson, G. Hong, Y. Liang, B. Zhang, O. Yaghi and H. Dai, "In Vivo Fluorescence Imaging in the Second Near-Infrared Window with Long Circulating Carbon Nanotubes Capable of Ultrahigh Tumor Uptake", *Journal of*

- the American Chemical Society*, vol. 134, no. 25, pp. 10664-10669, 2012. Available: 10.1021/ja303737a [Accessed 4 April 2019].
- [27] K. Welsher, S. Sherlock and H. Dai, "Deep-tissue anatomical imaging of mice using carbon nanotube fluorophores in the second near-infrared window", *Proceedings of the National Academy of Sciences*, vol. 108, no. 22, pp. 8943-8948, 2011. Available: 10.1073/pnas.1014501108 [Accessed 4 April 2019].
- [28] B. van Saders, L. Al-Baroudi, M. Tan and R. Riman, "Rare-earth doped particles with tunable infrared emissions for biomedical imaging", *Optical Materials Express*, vol. 3, no. 5, p. 566, 2013. Available: 10.1364/ome.3.000566 [Accessed 4 April 2019].
- [29] M. Zevon et al., "CXCR-4 Targeted, Short Wave Infrared (SWIR) Emitting Nanoprobes for Enhanced Deep Tissue Imaging and Micrometastatic Cancer Lesion Detection", *Small*, vol. 11, no. 47, pp. 6347-6357, 2015. Available: 10.1002/sml.201502202 [Accessed 4 April 2019].
- [30] H. Kantamneni et al., "Surveillance nanotechnology for multi-organ cancer metastases", *Nature Biomedical Engineering*, vol. 1, no. 12, pp. 993-1003, 2017. Available: 10.1038/s41551-017-0167-9 [Accessed 4 April 2019].
- [31] D. Naczynski et al., "Albumin Nanoshell Encapsulation of Near-Infrared-Excitable Rare-Earth Nanoparticles Enhances Biocompatibility and Enables Targeted Cell Imaging", *Small*, vol. 6, no. 15, pp. 1631-1640, 2010. Available: 10.1002/sml.200902403 [Accessed 4 April 2019].
- [32] O. Bruns et al., "Next-generation in vivo optical imaging with short-wave infrared quantum dots", *Nature Biomedical Engineering*, vol. 1, no. 4, p. 0056, 2017. Available: 10.1038/s41551-017-0056 [Accessed 4 April 2019].
- [33] G. Hong et al., "Multifunctional in vivo vascular imaging using near-infrared II fluorescence", *Nature Medicine*, vol. 18, no. 12, pp. 1841-1846, 2012. Available: 10.1038/nm.2995 [Accessed 4 April 2019].
- [34] E. Rosenthal et al., "Safety and Tumor Specificity of Cetuximab-IRDye800 for Surgical Navigation in Head and Neck Cancer", *Clinical Cancer Research*, vol. 21, no. 16, pp. 3658-3666, 2015. Available: 10.1158/1078-0432.ccr-14-3284 [Accessed 4 April 2019].
- [35] T. Kim, C. O'Brien, H. Choi and M. Jeong, "Fluorescence molecular imaging systems for intraoperative image-guided surgery", *Applied Spectroscopy Reviews*, vol. 53, no. 2-4, pp. 349-359, 2017. Available: 10.1080/05704928.2017.1323311 [Accessed 4 April 2019].
- [36] *Semrock - Part Number ICG-B*. 2019 [Online]. Available: <https://www.semrock.com/SetDetails.aspx?id=2786>. [Accessed: 04- Apr- 2019]
- [37] R. Zhang et al., "Beyond the margins: real-time detection of cancer using targeted fluorophores", *Nature Reviews Clinical Oncology*, vol. 14, no. 6, pp. 347-364, 2017. Available: 10.1038/nrclinonc.2016.212 [Accessed 4 April 2019].
- [38] M. Tan, J. Connolly and R. Riman, "Optical Efficiency of Short Wave Infrared Emitting Phosphors", *The Journal of Physical Chemistry C*, vol. 115, no. 36, pp. 17952-17957, 2011. Available: 10.1021/jp203735n [Accessed 4 April 2019].
- [39] *Zyla 5.5 sCMOS*. 2019 [Online]. Available: https://www.andor.com/pdfs/specifications/Andor_Zyla_5.5_and_4.2_PLUS_Specifications.pdf. [Accessed: 04- Apr- 2019]

- [40] *640HSX-1.7RT Legacy SWIR Camera*. 2019 [Online]. Available: http://www.sensorsinc.com/images/uploads/documents/VIS_NIR_SWIR_FPA_TYPICAL_QE_CHART.pdf. [Accessed: 04- Apr- 2019]
- [41] Y. Pu, L. Shi, S. Pratavieira and R. Alfano, "Two-photon excitation microscopy using the second singlet state of fluorescent agents within the “tissue optical window”", *Journal of Applied Physics*, vol. 114, no. 15, p. 153102, 2013. Available: 10.1063/1.4825319 [Accessed 4 April 2019].
- [42] M. Ogawa, N. Kosaka, P. Choyke and H. Kobayashi, "In vivo Molecular Imaging of Cancer with a Quenching Near-Infrared Fluorescent Probe Using Conjugates of Monoclonal Antibodies and Indocyanine Green", *Cancer Research*, vol. 69, no. 4, pp. 1268-1272, 2009. Available: 10.1158/0008-5472.can-08-3116 [Accessed 4 April 2019].